

# Multidirectional Mass Accretion and Collimated Outflows on Scales of 100–2000 au in Early Stages of High-mass Protostars

C. Goddi<sup>1,2</sup>, A. Ginsburg<sup>3</sup>, L. T. Maud<sup>4</sup>, Q. Zhang<sup>5</sup>, and Luis A. Zapata<sup>6</sup> Department of Astrophysics/IMAPP, Radboud University Nijmegen, P.O. Box 9010, NL-6500 GL Nijmegen, The Netherlands; c.goddi@astro.ru.nl, cgoddi@strw.leidenuniv.nl

ALLEGRO/Leiden Observatory, Leiden University, P.O. Box 9513, NL-2300 RA Leiden, The Netherlands 
 <sup>3</sup> Department of Astronomy, University of Florida, P.O. Box 112055, Gainesville, FL, USA 
 <sup>4</sup> European Southern Observatory, Karl-Schwarzschild-Str. 2, D-85748, Garching bei München, Germany 
 <sup>5</sup> Center for Astrophysics|Harvard & Smithsonian, 60 Garden Street, Cambridge, MA 02138, USA 
 <sup>6</sup> Instituto de Radioastronomía y Astrofisíca, UNAM, Morelia, Michoacán, C.P. 58089, México 
 *Received 2020 August 21; revised 2020 October 29; accepted 2020 October 30; published 2020 December 9*

#### **Abstract**

We observed the W51 high-mass star-forming complex with the Atacama Large Millimeter/submillimeter Array's longest-baseline configurations, achieving an angular resolution of ~20 mas, corresponding to a linear resolution of  $\sim 100$  au at  $D_{W51} = 5.4$  kpc. The observed region contains three high-mass protostars in which the dust continuum emission at 1.3 mm is optically thick up to a radius \$\leq 1000\$ au and has brightness temperatures \$\geq 200\$ K. The high luminosity ( $\gtrsim 10^4 L_{\odot}$ ) in the absence of free-free emission suggests the presence of massive stars  $(M \gtrsim 20 M_{\odot})$  at the earliest stages of their formation. Our continuum images reveal remarkably complex and filamentary structures arising from compact cores. Molecular emission shows no clear signs of rotation or infall on scales from 150 to 2000 au; we do not detect disks. The central sources drive young ( $t_{\rm dyn} \sim 100$  yr), fast ( $v \sim 100$  km s<sup>-1</sup>), powerful ( $\dot{M} > 10^{-4} \, M_{\odot} \, {\rm yr}^{-1}$ ), collimated outflows. These outflows provide indirect evidence of accretion disks on scales  $r \lesssim 100$ –500 au (depending on the object). The active outflows are connected to fossil flows that have different orientations on larger spatial scales, implying that the orientations of these small disks change over time. These results together support a variant of an accretion model for high-mass star formation in which massive protostars do not form a large, stable Keplerian disk during their early stages but instead accrete material from multiple massive flows with different angular momentum vectors. This scenario therefore contrasts with the simplified classic paradigm of a stable disk+jet system, which is the standard model for low-mass star formation, and provides experimental confirmation of a multidirectional and unsteady accretion model for massive star formation.

*Unified Astronomy Thesaurus concepts:* Jets (870); Star formation (1569); Circumstellar matter (241); Massive stars (732); Compact H II region (286); Stellar accretion disks (1579); Radio interferometry (1346); Long baseline interferometry (932); Stellar mass loss (1613); Stellar winds (1636); Stellar accretion (1578)

## 1. Introduction

The process by which high-mass young stellar objects (HMYSOs) accrete their mass is poorly understood. One fundamental issue is that, for HMYSOs, the timescale for gravitational contraction (the Kelvin-Helmholtz time,  $t_{KH} =$ 10<sup>3</sup>-10<sup>5</sup> yr) is shorter than the timescale for accretion. A consequent difficulty is that the star ignites nuclear burning reactions during its main accretion phase, which may turn on powerful feedback processes (such as radiation pressure, ionizing radiation, stellar winds, and outflows) that can halt or substantially reduce accretion. These processes are either absent or insignificant for low-mass stars. Different models have suggested that channeling material through a circumstellar accretion disk can overcome these feedback mechanisms (Krumholz et al. 2007, 2009; Kuiper et al. 2010, 2011; Seifried et al. 2011; Klassen et al. 2016). Despite the theoretical support, the observational evidence of disks around OB-type protostars was limited (e.g., Beltrán & de Wit 2016; Cesaroni et al. 2017), and, as a consequence, their existence was still a matter of debate until very recently.

Infrared (IR) interferometry has revealed disks on scales of less than 1000 au around a limited number of IR-bright HMYSOs (e.g., Kraus et al. 2010, 2017; Boley et al. 2013; Frost et al. 2019). These HMYSOs are, however, relatively

evolved and have apparently accreted most of their mass. Furthermore, IR interferometry data alone cannot constrain the total extent of those disks, which requires observations at longer wavelengths (e.g., Beltrán & de Wit 2016). In this context, observations with (sub)millimeter (millimeter) interferometers allow access to more embedded (i.e., less evolved) HMYSOs and have led in recent years to the identification of about a dozen disk candidates with Keplerian signatures around luminous HMYSOs (we report a full list of the disk sources, their properties, and relevant references in Appendix E and Table 3). Among the clearest cases, we mention the archetypal B-type protostar IRAS 20126+4104 (Cesaroni et al. 2014), the closest-known HMYSO Orion Source I (Ginsburg et al. 2018), and the YSO G16.59-0.05 (Moscadelli et al. 2019). In particular, with the advent of the Atacama Large Millimeter/ submillimeter Array (ALMA) with its longest baselines, the evidence for Keplerian-like disks around O-type HMYSOs has been increasing, including G17.64+0.16 (Maud et al. 2018, 2019), G11.92-0.61 (Ilee et al. 2018), G023.01-00.41 (Sanna et al. 2019), and IRAS 16547-4247 (Zapata et al. 2019). Besides interferometric observations of millimeter thermal lines, very long baseline interferometry (VLBI) studies have revealed that maser emission lines trace accretion structures and disk winds in the circumstellar environments

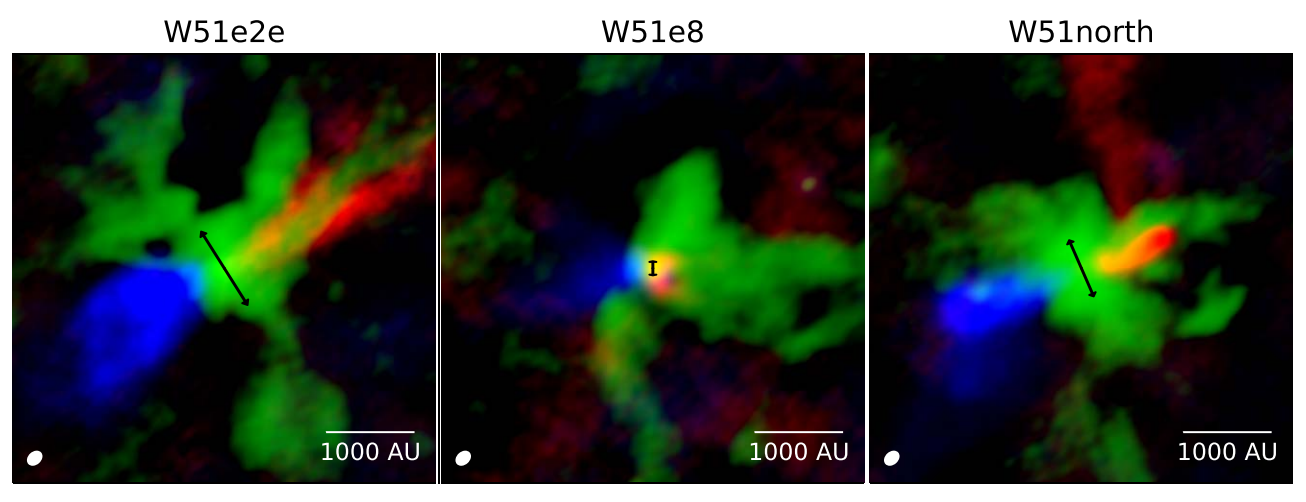


Figure 1. Overlays showing the complex structures in the circumstellar material around the high-mass protostars W51e2e, W51e8, and W51north (from left to right). The three-color images show the dust continuum emission at  $\lambda$ 1.3 mm (in green), tracing warm dust (50–400 K) in the (accreting) cores, and the redshifted and blueshifted emission of the SiO J=5-4 line (in red and blue), tracing fast gas ( $\pm$ 100 km s<sup>-1</sup>) outflowing material from the same cores. An area of 5000  $\times$  5000 au is plotted in each panel, centered on  $\alpha$ (J2000) =  $19^{h}23^{m}43^{s}.9659$ ,  $\delta$ (J2000) =  $+14^{\circ}30'34''.499$  (W51e2e),  $\alpha$ (J2000) =  $19^{h}23^{m}43^{s}.904$ ,  $\delta$ (J2000) =  $+14^{\circ}31'05''.483$  (W51north), respectively (see Figures 8 and 9 in Appendix B for absolute coordinates). The black arrows indicate the orientation and the upper limits to the size of the putative underlying disks. The angular resolution of the continuum emission data is given by the ellipse drawn in the lower left corner ( $0''.033 \times 0''.024$  or 178 au  $\times$  130 au).

of HMYSOs (e.g., Matthews et al. 2010; Sanna et al. 2010; Goddi et al. 2011a; Moscadelli & Goddi 2014).

Despite the growing evidence on both the theoretical and observational sides, it is still somewhat unclear whether the dozen identified disklike structures are similar to their low-mass counterparts, dominated by the central YSO and in Keplerian rotation, or are self-gravitating, nonequilibrium rotating entities. The two structures may also coexist as a stable inner Keplerian disk embedded in a larger self-gravitating rotating envelope. In principle, even more complex pictures are possible for HMYSOs. For instance, recent 3D (magneto)hydrodynamic (MHD) simulations of collapsing high-mass gas cores have shown that accretion on 1000 au scales is through filaments rather than a large disk (Commercon et al. 2011; Myers et al. 2013; Seifried et al. 2015). These filaments act as accretion streams that feed smaller Keplerian disks that are allowed to only form on scales of order  $r \lesssim 100$  au (Seifried et al. 2012, 2013, 2015; Joos et al. 2013; Myers et al. 2013; Rosen et al. 2016, 2019). This mechanism allows the star to sustain high average accretion rates (of order of  $10^{-3} M_{\odot} \text{ yr}^{-1}$ ) while mitigating the effects of stellar feedback. This theoretical prediction has never been confirmed via observations. The fundamental question of how the highest-mass proto-O stars gather their mass therefore remains open. To test these exciting predictions on the formation mechanism for the most massive stars, observations with a spatial resolution of order of 100 au targeting pre-main-sequence HMYSOs that are vigorously accreting are required.

With this in mind, we have used ALMA to study the highmass star-forming complex W51 at 1.3 mm with its longest baselines of 16 km. The W51 complex ( $D \sim 5.4$  kpc; Sato et al. 2010) is among the most luminous star-forming regions in the galaxy ( $L \sim 2 \times 10^7 L_{\odot}^{-7}$ ; Ginsburg et al. 2016) and is forming a very massive protocluster (>10<sup>4</sup>  $M_{\odot}$ ; Ginsburg et al. 2016), with over 100 protostellar sources detected (Ginsburg et al. 2017). The protocluster contains both exposed O-type stars (Rivera-Soto et al. 2020) and deeply embedded HMYSOs (Ginsburg et al. 2017), and as such, it is a powerful laboratory for studying the entire high-mass star formation process.

Here we focus on three HMYSOs, W51e2e, W51e8, and W51north, which are distributed across an  $\sim$ 3 pc region. Previous observational studies using the JVLA (Goddi et al. 2015, 2016; Ginsburg et al. 2016) and ALMA cycle 2 (Ginsburg et al. 2017) have provided kinematic and physical properties of these HMYSOs on angular scales of 0."2-1."0 (corresponding to 1000-5000 au). These authors have also ruled out the presence of an observable ionized (H II) region toward each of these targets down to a low ionizing continuum luminosity limit, indicating that the central sources have not yet started ionizing their surroundings via ultraviolet radiation and therefore must be in the earliest stages of their evolution. The longest baselines at 1.3 mm provide an angular resolution of 20-30 mas, which allows us to unveil complex structures in the circumstellar material, as well as collimated outflows at radii 100-2000 au, showcased in Figure 1, and thus to investigate the mass accretion mechanism on the relevant scales to test theoretical models.

This paper is structured as follows. Section 2 summarizes the observations, data reduction, and imaging of both the 1.3 mm continuum emission and selected molecular lines tracing dense gas and outflows. Section 3 describes the data analysis aimed at deriving the physical (masses, temperatures, and luminosities) and kinematic (rotation, infall, and outflow) properties of the observed HMYSOs. Section 4 highlights the main results on the accretion/outflow structures identified in our high angular resolution images. In Section 5, we discuss the implications of these measurements in the context of our current theoretical understanding of high-mass star formation. Conclusions are drawn in Section 6.

## 2. Observations, Data Reduction, and Imaging

## 2.1. Observations

As part of the ALMA cycle 3 program 2015.1.01596.S, we observed two fields centered on W51north ( $\alpha$ (J2000) =

<sup>&</sup>lt;sup>7</sup> This luminosity is estimated using Herschel Hi-Gal within a 2 pc radius, which includes both the W51 IRS2 and W51 main protoclusters (see Ginsburg et al. 2016 for details).

 $19^{\text{h}}23^{\text{m}}40^{\text{s}}05$ ,  $\delta(\text{J}2000) = +14^{\circ}31'05''.5$ ) and W51e2/e8  $(\alpha(J2000) = 19^{h}23^{m}43^{s}91, \delta(J2000) = +14^{\circ}30'34''.6)$  with long baselines in Band 6 (216–237 GHz). The project was carried out in three executions on 2015 October 27 and 30. Between 37 and 42 antennas in the 12 m array were employed and provided baselines ranging from 85 to 16,196 m. The precipitable water vapor was between 0.85 and 1.98 mm for the observations, and there was reasonable phase stability (see below). We employed the Band 6 sideband-separating receivers in dual polarization mode to record nine spectral windows (SPWs). Seven SPWs had an ~234 MHz bandwidth, were recorded with 960 channels, and were Hanning smoothed by a factor of 2, achieving a frequency resolution of 564 kHz (corresponding to  $\sim 0.75$  km s<sup>-1</sup> at Band 6). This setup enabled us to cover a large number of spectral lines from different molecular species. The remaining two SPWs had a broader bandwidth of 1.8 GHz and a frequency resolution of 1.13 MHz (corresponding to  $\sim$ 1.5 km s<sup>-1</sup>) to obtain sensitive continuum measurements at 217 and 235 GHz, as well as to cover additional spectral lines. We spent 2.2 hr on-source during a total observing time of 5.3 hr.

## 2.2. Data Reduction and Imaging

The data calibration and imaging was carried out in the Common Astronomy Software Applications (CASA) package (version 4.5.1) and followed standard procedures. Fast referencing was used for these long-baseline observations; the phase calibrator was observed every  $\sim 70 \,\mathrm{s}$ . The phase calibrator-to-target field separation angle was small at  $<1^{\circ}2$ . The combination of fast switching times and a close phase calibrator is imperative for accurate phase calibration interpolation for these long baselines. Additionally, the water vapor radiometer (WVR) scaling algorithm (Maud et al. 2017) was implemented to improve the short-term (3–6 s) phase stability. This is a stand-alone modular package that runs inside the CASA environment and provides a user with the optimal value to scale the water vapor corrections in the WVRGCAL task within CASA. The phase calibration of the data was then further improved by phase self-calibrating on the continuum emission down to an integration timescale of 50 s (using the CASA tasks tclean and gaincal). The combined effect of WVR scaling and phase self-calibration improved the dynamic range of the final continuum maps by about 35%. The self-calibration solutions from the continuum were also applied to the full spectral data set (using the CASA task applycal) in order to improve the signal-to-noise ratio of the line cubes.

The calibrated visibilities were transformed from the Fourier plane (uv domain) into the image domain using the tclean algorithm. Three sets of images were produced using uniform, Briggs (robust parameter R=0.5), and natural weighting schemes that achieved angular resolutions of  $\sim 19$ , 28, and 35 mas, respectively. Since interferometric observations lead to spatial filtering of large-scale structures, the maximum recoverable scale in our images is  $0.^{\prime\prime}4$  (about 2000 au at a distance of 5.4 kpc). This implies that we do not detect any emission that is extended over scales larger than 2000 au. In our images, we only include data from baselines longer than 300 m to mitigate striping in the images from large-scale emission detected on the shortest baseline that could not be properly imaged (baselines with a length below this value being predominantly in one direction).

#### 2.2.1. Continuum Emission

Continuum images were produced by selecting line-free channels in each SPW and then combining all SPWs and have a resulting central frequency of about 226 GHz, assuming a flatspectrum source. Channel selection was accomplished in the uv domain using the shorter baselines, <1000 m, where emission is seen and line-free regions can be discerned. Approximately 5% of the total bandwidth was assessed to be "line-free" and selected to establish the continuum level. The final images were cleaned to a threshold of 0.3 mJy and then corrected for the primary beam response. The lowest noise level in the images, away from bright sources, is typically  $\sim 0.1 \,\mathrm{mJy\ beam^{-1}}$ , near the thermal noise level, as expected from the ALMA sensitivity calculator (near the brightest sources, W51e2e and W51north, the noise can be two to three times higher). Continuum images were produced with both uniform and Briggs weighting with a robust parameter R = 0.5, achieving resolutions of  $\sim 19$  and 28 mas, respectively. The former provides the highest angular resolution to identify compact components, while the latter provides comparably better signal-to-noise ratios to recover the filamentary structure around the dusty peaks (displayed in Figure 1).

#### 2.2.2. Line Emission

We produced spectral image cubes of each SPW. For the emission line analysis, we used natural weighting (also excluding baselines shorter than 300 m) in order to provide the highest signal-to-noise ratio, yielding a typical angular resolution of 35 mas. Images were also produced using a Briggs robust = 0.5 weighting that were useful in identifying more compact components. The typical rms noise level was  $\sim 1 \text{ mJy beam}^{-1}$  in line-free channels and  $\sim 2 \text{ mJy beam}^{-1}$  in channels with strong line emission.

The kinematic and moment analysis was performed outside of CASA. First, the median value over the full SPW was used to estimate and subtract the local continuum (Sanchez-Monge et al. 2018). Second, from the full-SPW cubes, we extracted cubes of all of the identified spectral lines using the Astropy module spectral-cube. Third, for selected lines, we created integrated intensity (zeroth-moment), velocity (first-moment), and velocity dispersion (second-moment) maps. The first- and second-moment maps were constructed using an intensity threshold of 7 mJy ( $\sim 3\sigma - 4\sigma$ , depending on spectral channel/source), and the velocity extent was chosen to avoid contamination from nearby lines where possible.

## 3. Results and Analysis

### 3.1. Dust Continuum Sources

Figure 2 shows the 1.3 mm continuum emission, in units of brightness temperature ( $T_B$ ), tracing warm dust in the W51e2e, W51e8, and W51north hot cores. The dust emission is resolved into complex structures and displays multiple components on scales of 100–3000 au. In the following, we estimate sizes (Section 3.1.1) and masses (Section 3.1.2) of different components, as well as luminosities (Section 3.1.3) of the three dusty sources.

## 3.1.1. Sizes

W51e2e.—The dust emission is centrally peaked (at  $T_{B,\rm max}=575$  K). Around the brightest central beam, the dust emission exhibits a clear central core object that is circular with a radius of  $r\approx500$  au (visualized by the orange contour at

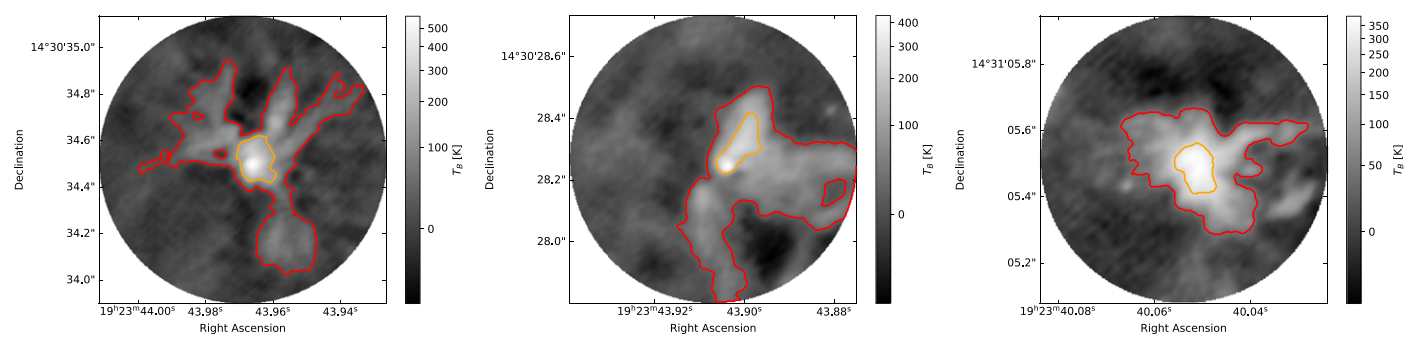


Figure 2. The gray scale shows the dust continuum emission, tracing warm dust in the W51e2e, W51e8, and W51north hot cores (from left to right). The contours enclose the regions where we compute the mass values quoted in the paper for both the central cores (orange contours) and the full extent of the continuum (red contours). In particular, the orange and red contours trace the 23% and 3% (131 and 15 K), 35% and 3% (152 and 15 K), and 62% and 10% (245 and 39 K) levels from the continuum flux density peaks of 19, 14, and 13 mJy beam<sup>-1</sup> for W51e2e, W51e8, and W51north, respectively. The brightness temperature  $T_B$  scale is on the right-hand side in each panel.

 $T_B = 130 \,\mathrm{K}$  in Figure 2). In the larger area around W51e2e, there are four main filamentary structures that extend out to  $r \sim 2700 \,\mathrm{au}$  (seen as the red contour at  $T_B = 15 \,\mathrm{K}$  in Figure 2).

W51e8.—The dust emission is centrally peaked (at  $T_{B,\max}$  = 435 K). Fitting a Gaussian model to the continuum emission peak in both the uniform and Briggs maps provides a consistent deconvolved FWHM size of 0."028 (150 au). The structure surrounding the bright central source is less symmetric than W51e2e. A filament extends from the peak to 1200 au along the northwest (NW; captured by the orange contour at  $T_B = 152$  K in Figure 2). There is also a more extended structure toward the southwest (SW), covering approximately a semicircle centered on the brightest central peak out to a maximum radius of 2500 au (seen as the red contour at  $T_B = 15$  K in Figure 2).

W51north.—At variance with W51e2e and W51e8, the dust emission in W51north does not contain a central bright point source but displays a slightly elongated peanut-shaped structure with homogeneous brightness (shown with orange contour at  $T_B = 245 \text{ K}$  in Figure 2). Fitting a Gaussian model in both the uniform and Briggs maps provides a consistent deconvolved FWHM long axis of 0."130 (700 au). The larger surrounding structure (captured in the red contour at  $T_B = 39 \text{ K}$  in Figure 2) is contained within a 1200 au radius and is primarily elongated northeast (NE)–SW.

## 3.1.2. Masses

For the mass estimates, we make a distinction between optically thick and optically thin emission.

We first assume that in the highest column density regions (i.e., toward the source centers), the sources are just barely optically thick ( $\tau=1$ ). Therefore,  $N({\rm H_2})=\tau/\kappa_{\nu}=1/\kappa_{\nu}$ , where  $\kappa_{\nu}$  is the dust opacity coefficient. We use the same coefficient,  $\kappa_{227~\rm GHz}=0.0083~\rm cm^2~g^{-1}$ , as in Ginsburg et al. (2017), resulting in  $N({\rm H_2})=2.6\times10^{25}~\rm cm^{-2}$ . The mass in a beam is then  $M_{\rm beam}=N({\rm H_2})\times A=A/\kappa$ , where A is the beam area (0.033  $\times$  0.024) in cm<sup>2</sup>, which yields dust masses of each source  $M_{\rm beam}=0.36~M_{\odot}$ .

Although the highest column density peak positions have increased optical depth, the emission surrounding the peak position is likely to be optically thin. We can then use the flux density measurements to compute gas masses using the

following equation:

$$M = \frac{S_{\nu}d^2}{\kappa_{\nu}B_{\nu}(T_d)},$$

where  $S_{\nu}$  is the source flux density, d is the distance to the source,  $\kappa_{\nu}$  is the dust opacity coefficient (which includes the gas-to-dust ratio of 100), and  $B_{\nu}(T_d)$  is the Planck function for a blackbody at dust temperature  $T_d$ . The latter is not known, but we can estimate lower limits to  $T_d$  in two different ways. The first estimate is provided by the peak brightness temperature of the millimeter continuum emission at the source center (where we assume that the emission is optically thick). The peak intensities of the three sources in the robust 0.5 maps are  $S_{227 \text{ GHz}}(\text{e2e}) = 19.4$ ,  $S_{227 \text{ GHz}}(e8) = 14.7$ , and  $S_{227 \text{ GHz}}(\text{north}) = 13.2 \text{ mJy beam}^{-1}$ , which correspond to brightness temperatures of  $T_{B,\text{max}} = 575$ , 435, and 390 K, respectively. These provide the first lower limits on  $T_d$ . A second estimate comes from LTE modeling of CH<sub>3</sub>OH lines imaged with the ALMA cycle 2 program (Ginsburg et al. 2017), which provided temperatures in the range 200–600 K inside 5000 au. Therefore, we can assume  $T = T_{\text{gas,min}} = 200 \text{ K}$ as a second lower limit on  $T_d$ .

In the following, we use these two approaches (assuming thin and thick emission) and independent  $T_d$  lower limits to obtain mass estimates of the spatially resolved cores.

W51e2e.—The central core object spans 27 beam areas (radius  $r\approx 500$  au), implying a mass  $M_{\rm e2e,core}=0.36\times 27=9.7~M_{\odot}$  if it is entirely optically thick. If it is optically thin, on average, using the expression above for  $T_d=T_{B,\rm max}=575~{\rm K}$ , the total is 4  $M_{\odot}$ , while for  $T_d=T_{\rm gas,min}=200~{\rm K}$ , the total is 12  $M_{\odot}$ . In the surrounding filamentary structures, we estimate the mass assuming  $T_d=200~{\rm K}$  and obtain  $M_{\rm e2e,filaments}=25~M_{\odot}$  (excluding the inner core).

W51e8.—For the filament extending to 1200 au from the central peak along the NW, we measure a mass of 4  $M_{\odot}$  for  $T_d = T_{B,\rm max} = 435$  K and 9  $M_{\odot}$  for  $T_d = T_{\rm gas,min} = 200$  K. For extended structure toward the SW, we obtain  $M(200~K) = 16~M_{\odot}$ .

W5Inorth.—The central peanut-shaped structure occupies 14 beams, implying a lower-limit mass  $M_{\rm north,core}=0.36\times14=5$   $M_{\odot}$  if it is optically thick or  $M=4.2~M_{\odot}$  if it is optically thin and isothermal at  $T_d=T_{B,\rm max}=390~{\rm K}$ . For the larger surrounding structure, we obtain a mass range  $M(390~{\rm K})=14~M_{\odot}$  and  $M(200~{\rm K})=28~M_{\odot}$ .

 Table 1

 Properties of the 1.3 mm Dusty Sources Associated with HMYSOs W51e2e, W51e8, and W51north

Source		Central Beam		Compact Core		Extended Structure		Dust	Protostellar
		Radius (au)	Mass $(M_{\odot})$	Radius (au)	Mass $(M_{\odot})$	Radius (au)	Mass $(M_{\odot})$	<del>-</del>	$\frac{\text{Luminosity}^{\text{a}}}{(L_{\odot})}$
W51e2e <sup>b</sup>		70	0.36	500	4–12	2700	25	575	$> 8.2 \times 10^3$
W51e8 <sup>c</sup>		75	0.36			2500	16	435	$>7.5 \times 10^{3}$
W51north <sup>d</sup>	•••	•••	•••	350	4–5	1200	14–28	390	$>2.8 \times 10^{3}$

Notes. The sizes and masses are estimated for different components of the dust continuum emission.

Table 1 summarizes the sizes and masses of the different components: centrally peaked core, surrounding compact core, and filaments.

We compare the recovered flux in the long-baseline maps to that in the ALMA cycle 2 maps at the same frequency (Ginsburg et al. 2017). In the robust 0.5 maps, in W51e2e, 13% of the flux is recovered; in W51e8, 12%; and in W51north, 23%. These low recovery fractions indicate that most of the dust emission is smooth on  $\gtrsim$ 2000 au scales. It is therefore likely that the cores reside in a larger envelope of dense material containing up to 5–10 times as much mass within  $r \lesssim$  2000 au as we have estimated above (Ginsburg et al. 2017).

#### 3.1.3. Protostellar Luminosities

The peak brightness temperatures are a lower limit to the surface brightness of the millimeter core, since an optical depth  $\tau < 1$  or a filling factor of the emission ff < 1 would both imply higher intrinsic temperatures. One can use these temperatures to estimate lower limits on the source luminosities. Assuming blackbody emission from a spherical beam-filling source, the luminosity can be calculated as  $L = 4\pi r^2 \sigma_{\rm sb} T^4$ , where  $\sigma_{\rm sb} = 5.670373 \times$  $10^{-5}$  g s<sup>-3</sup> K<sup>-4</sup> is the Stefan–Boltzmann constant. This provides lower limits of  $8.2 \times 10^3$ ,  $7.5 \times 10^3$ , and  $2.8 \times 10^3$   $L_{\odot}$  for the luminosity of W51e2e, W51e8, and W51north, respectively. Such luminosities correspond to B1–B1.5V main-sequence stars with masses  $M \sim 8-11~M_{\odot}$  and effective temperatures of 24,000–26,000 K (Pecaut & Mamajek 2013). However, the coarser-resolution observations carried out with ALMA in cycle 2 recovered more flux within a 0"2 radius, yielding slightly higher luminosities,  $L \gtrsim 10^4 L_{\odot}$ , implying masses  $M \gtrsim 10$ –15  $M_{\odot}$ (Ginsburg et al. 2017). Even these larger-scale measurements are luminosity lower limits, as an unknown fraction of the luminosity escapes to much larger radii along the outflow cavities without being reprocessed by dust.

## 3.2. Kinematics of Dense Molecular Gas

Each of the three target sources is a typical hot molecular core and extremely rich in spectral lines (see Ginsburg et al. 2017). Within the plethora of identified spectral lines, we identified a subset of lines that are unblended and strong enough to be used for kinematic analysis. The molecular lines observed directly toward the dusty structures are only seen in absorption against the continuum, with the exception of SiO, which is seen in the outflow (see Section 3.3).

In order to study gas kinematics, we used intensity-weighted velocity maps and velocity dispersion maps of different dense gas tracers, which achieve a typical spatial resolution of about 150-200 au. In Figure 4, we display velocity field maps for selected lines of CH<sub>3</sub>CN<sup>8</sup> for W51e2e, W51e8, and W51north. A remarkable feature seen in these velocity maps is the nearly perfectly flat velocity field in all three sources near their systemic velocity (shown in green). This property is best seen toward W51north, where different CH<sub>3</sub>CN lines from the K-ladder (with lower energy levels between 122 and 515 K) show exactly the same remarkably flat velocity profile regardless of their excitation (Figure 4, bottom row). This result does not depend on the molecular tracers or probed scales and thus mirrors real physical properties of the targeted HMYSOs. The only exception is W51e2e (Figure 4, top left panel), which shows redshifted velocities along the NW dust lane (see Section 4.1 for an interpretation).

In Appendix A, we review possible explanations for the lack of velocity structure toward these cores, and we conclude that it is an observational effect caused by the high optical depth in the dust continuum, as predicted in Krumholz et al. (2007).

## 3.3. Protostellar Outflows

We detected bright SiO ( $J = 5\text{--}4 \ v = 0$  line) emission that traces compact bipolar outflows stemming from the three HMYSOs. These small-scale SiO outflows are barely detected beyond  $r \sim 2000$  au, but they connect to larger-scale outflows (2000–30,000 au) detected in  $^{12}$ CO ( $J = 2\text{--}1)^9$  by Ginsburg et al. (2017). The outflows from W51e2e and W51north are shown in Figures 5 and 6 (see Appendix B for a detailed description of their structures).

Both CO and SiO outflows display high speeds (with peak velocities  $\pm 100~\rm km~s^{-1}$ ). Such high speeds coupled with the compact sizes imply that these outflows are dynamically very young. In particular, the CO outflows have a dynamical age of a few thousand years, whereas the SiO outflows have a dynamical age of roughly 100 yr (see Appendix C.1 for dynamical age estimates).

While the W51e2e outflow has a simple bipolar morphology, the W51north outflow shows a sharp change from small to

<sup>&</sup>lt;sup>a</sup> These protostellar luminosities are lower limits, as inferred in Section 3.1.3.

b In W51e2e, the mass estimate in the extended filamentary structure does not include the inner core.

<sup>&</sup>lt;sup>c</sup> In W51e8, there is no core-like symmetric structure surrounding the bright central source.

<sup>&</sup>lt;sup>d</sup> W51north does not contain a central bright point source.

<sup>&</sup>lt;sup>8</sup> CH<sub>3</sub>CN is a typical dense gas tracer (e.g., Cesaroni et al. 2017) and often seen to trace rotation in disklike structures (Johnston et al. 2015; Ilee et al. 2018), although this is not always the case (Maud et al. 2018).

 $<sup>^{9}</sup>$  Shi et al. (2010b) also mapped the outflow from W51e2e in the  $^{12}$ CO J=3–2 line.

Table 2
Outflow Parameters Derived from the SiO (J = 5–4) Line Emission in W51north, W51e2e, and W51e8

Source (1)	$\frac{\Delta V}{(\text{km s}^{-1})}$ (2)	$V_{\text{max}} \\ (\text{km s}^{-1}) \\ (3)$	R <sub>max</sub> (au) (4)	T <sub>dyn</sub> (yr) (5)	I <sub>int</sub> (K km s <sup>-1</sup> ) (6)	<i>M</i> ( <i>M</i> <sub>☉</sub> ) (7)	$P \qquad (M_{\odot} \text{ km s}^{-1}) \qquad (8)$	$(M_{\odot} \text{ yr}^{-1} \text{ km s}^{-1})$ (9)	$\dot{M}_{\rm ejection}$ $(M_{\odot} {\rm yr}^{-1})$ $(10)$
W51north	[-36, 56]	95	1540	77	$1.39 \times 10^4$	0.18	9.2	0.12	$2.4 \times 10^{-4}$
W51e2e W51e8	[-56, 53] [0, 60]	105 42	2560 390	116 44	$1.34 \times 10^4$ $0.94 \times 10^4$	0.36 0.11	24.8 1.5	0.21 0.03	$4.3 \times 10^{-4}$ $0.7 \times 10^{-4}$

**Note.** The parameters are estimated from the blueshifted lobe. The total outflow mass and rate are twice the quoted values. To convert from the SiO column to the  $H_2$  column, we assume a conservatively high abundance of SiO,  $X_{SiO} = N(SiO)/N(H_2) = 10^{-7}$ . A lower  $X_{SiO}$  would imply higher mass and momentum in the outflow. The age estimates assume an inclination angle of  $45^{\circ}$ . For an inclination *i*, the values need to be multiplied by a factor  $\cos(45^{\circ})/\cos(i)$ .

large scales. The inner SiO outflow is simple and bipolar at a position angle (P.A.) of  $-70^{\circ}$  out to r < 1300 au, at which point the redshifted flow is sharply truncated (the blueshifted lobe extends out to  $r \le 1600$  au). Starting at about 800 au from the center, the redshifted SiO emission suddenly turns by  $80^{\circ}$  (at a P.A. of  $\sim 10^{\circ}$ ) and continues to the north out to  $\sim 5000$  au, where it meets the large-scale <sup>12</sup>CO outflow, which extends out to  $\sim 20,000$  au at a P.A. of  $\sim 13^{\circ}$ . The outflow is also detected in H<sub>2</sub>O maser emission, which consistently traces the SiO morphology and kinematics (Imai et al. 2002; Figure 6, lower panel).

We discuss possible scenarios to explain this peculiar outflow structure in Section 4.4.

## 3.4. Momentum and Ejection Rates of Outflows

We can use the SiO emission structure to estimate the momentum and ejection rates of the outflows. One straightforward method would be to determine the mass of the outflowing gas from SiO emission and divide it by the outflow dynamical age. While this may provide the correct order-of-magnitude answer in some cases, molecular outflows, such as those seen in CO and SiO emission, are driven by an underlying primary wind/jet and probe mostly entrained ambient gas moving at lower velocity (this applies especially to CO).

Since in protostellar jet/outflow systems, momentum is conserved (we assume momentum-driven outflows; e.g., Masson & Chernin 1993), one can set a tight constraint on the mass-loss rate using  $\dot{m}_j v_j = \dot{m}_o v_o = \dot{P}_o$ , where  $\dot{m}$  is the mass-loss rate, v is the speed, and  $\dot{P}$  is the momentum rate (j and o stand for the primary jet and molecular outflow, respectively).

The outflow momentum rate can be obtained by dividing the outflow momentum by its age. In Appendix C.1, we estimate the dynamical age of the outflows from the ratio of their projected length to their maximum speed by assuming an inclination  $i = 45^{\circ}$ . In Appendix C.2, we estimate the momentum of the outflowing gas by computing its mass from the SiO emission integrated in the full velocity range. In order to convert from the SiO column to the H<sub>2</sub> column, we need to fix the abundance of SiO,  $X_{SiO} = N(SiO)/N(H_2)$ . Toward a sample of 14 high-mass star-forming regions, Leurini et al. (2014) used the APEX singledish telescope to target the SiO (J=3–2 and J=8–7) lines, obtaining  $X_{\rm SiO}=(0.7$ –4.8)  $\times$   $10^{-8}$ , while Sánchez-Monge et al. (2013b) used the IRAM 30 m telescope to target the same sample in the SiO (J=2-1 and J=5-4) lines, obtaining  $X_{\rm SiO}=(0.1-3)\times 10^{-8}$ . We assume a conservatively high abundance of SiO  $X_{\rm SiO}=10^{-7}$  (a lower abundance of SiO would imply higher mass and momentum in the outflow). The ages, momenta, and resulting momentum rates derived with this analysis are reported in columns 5, 7, and 8 of Table 2,

respectively. The momentum analysis was conducted on the blueshifted lobes (which display a simpler structure; see Appendices B and C.2); therefore, the total outflow mass and momentum rate are found by multiplying those numbers by a factor of 2 (to account for both outflow lobes), yielding  $M_o = 0.72$ , 0.36, and 0.22  $M_{\odot}$  and  $\dot{P}_o = 0.42$ , 0.24 and 0.06  $M_{\odot}$  yr<sup>-1</sup> km s<sup>-1</sup> for the outflows driven by W51e2e, W51north, and W51e8, respectively. Using the  $^{12}\text{CO }J = 3-2$  line, Shi et al. (2010b) found a larger outflow mass of 1.3  $M_{\odot}$  and a lower momentum rate of 0.04  $M_{\odot}$  yr<sup>-1</sup> km s<sup>-1</sup> for W51e2 (both estimates use only the blueshifted lobe). Their larger mass is not surprising, since  $^{12}\text{CO}$  probes swept-up ambient gas on much larger scales ( $\gtrsim$ 2" or  $\gtrsim$ 10,000 au versus  $\lesssim$ 2600 au), while a lower momentum rate is expected for a much older fossil outflow (with an age of about 1600 yr versus 115 yr for the SiO outflow).

At this point, we can convert the computed momentum rates of the molecular outflows into the ejection rates of the primary winds/jets. This requires knowledge of their speed, which, however, we do not measure. Jet speeds measured in low-mass outflows via spectroscopy of atomic lines in the optical and near-IR wavelengths are typically a few hundred kilometers per second (e.g., Frank et al. 2014). For massive outflows, there are fewer measurements of jet velocities, but a handful of propermotion studies of the radio continuum jets provide speeds of about 500 km s<sup>-1</sup> (e.g., HH 80/81; Marti et al. 1995). Using the total momentum rates computed above, we derive the following mass ejection rates for the primary jet:  $\dot{m_j} = \left[\frac{v_j}{500 \text{ (km s}^{-1})}\right] \times \left[\frac{\cos 45^{\circ}}{\cos(i)}\right] \times 8.6 \times 10^{-4} M_{\odot} \text{ yr}^{-1} \text{ in}$ W51e2e,  $4.8 \times 10^{-4} M_{\odot} \text{ yr}^{-1}$  in W51north, and  $1.4 \times 10^{-4}$  $M_{\odot}$  yr<sup>-1</sup> in W51e8, where *i* is expressed in units of degrees and  $v_i$  is the jet speed in kilometers per second. We emphasize that the estimate for W51e8 is less reliable owing to its high apparent inclination (we detect red- and blueshifted emission

### 4. Discussion

on both sides of the central protostar, indicating  $i < 45^{\circ}$ ).

The analysis of the ALMA long-baseline images presented in the previous section yields four main findings.

- 1. There are warm (≥50–150 K) dusty filaments converging onto compact cores (Figures 1–3) that we suggest are accretion flows (Section 4.1).
- 2. We find no hints of rotation toward these cores (Figure 4), suggesting that they do not host large disks ( $R_{\text{max}}$ <75, <350, and <500 au for e8, north, and e2e, respectively; Section 4.2).

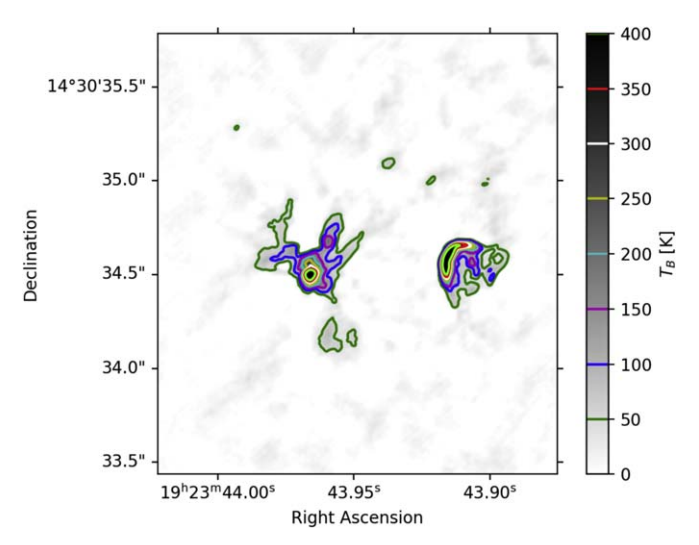


**Figure 3.** The gray scale shows the 1.3 mm continuum emission, tracing warm dust in the W51e2 core. The dusty hot core e2e is to the left, and the hypercompact H II region e2w (not discussed in this article) is to the right. The contours enclose the regions with different brightness temperatures  $T_B$  (scale on the right-hand side). While the highest temperatures in e2e are measured toward the central core, the dusty streamers are also significantly warm, with 50–150 K.

- 3. The central sources in the cores drive young ( $\sim$ 100 yr), compact ( $\lesssim$ 2000 au), fast ( $\sim$ 100 km s<sup>-1</sup>), powerful ( $10^{-3}$   $10^{-4}~M_{\odot}~\rm yr^{-1}$ ), collimated SiO outflows (Figures 5 and 6), indicating that the driving protostars are vigorously accreting (Section 4.3).
- 4. The outflow from W51north has a different axis (projected onto the plane of the sky) as a function of distance from the protostar (Figure 6), hinting at a change of direction over time (Section 4.4).

In the following, we discuss these findings in detail.

### 4.1. Dusty Streamers as Accretion Channels

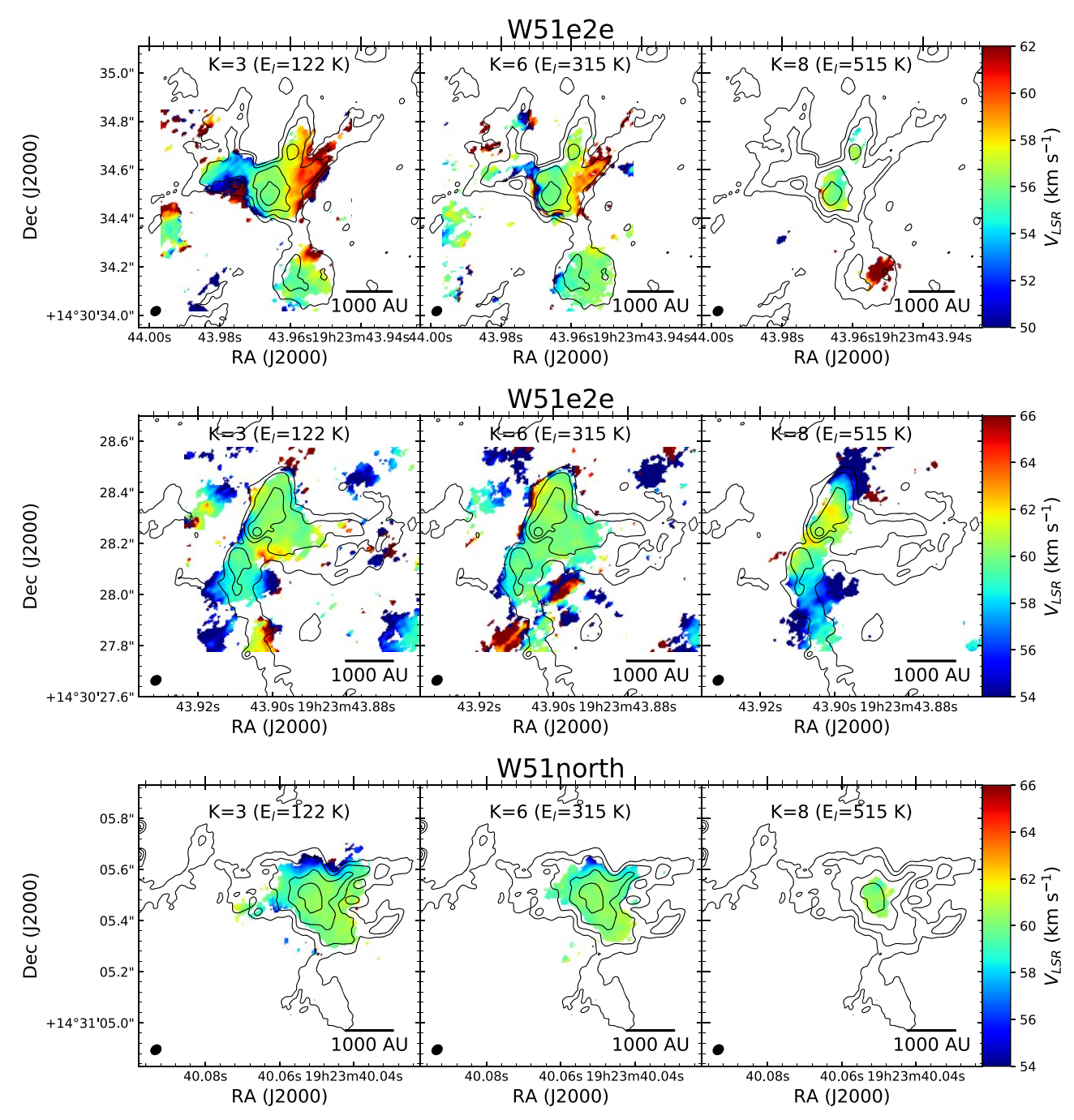
Lack of kinematic signatures of accretion.—Having identified these dusty streamers, we attempted to determine their kinematics to assess their nature, in particular to distinguish between material that is plunging into the cores (infall) or being flown out (outflow). Unfortunately, we do not identify any clear kinematic signatures toward them (Section 3.2 and Figure 4). The only exception is W51e2e (Figure 4, left panel), which shows redshifted velocities along the NW dust lane. Since these lines are seen in absorption against the dust continuum, one would be prompted to conclude that they probe dense gas infalling toward the compact core. However, the redshifted velocities are observed away from the dust continuum peak and

only along the redshifted lobe of the SiO outflow, which is pointing away from us, suggesting that this material may actually be entrained by the outflow. In this scenario, the lower opacity expected along the outflow cavity may explain why dense gas tracers like CH<sub>3</sub>CN display kinematics only along that specific line of sight.

Are the dust lanes outflow rather than accretion flows?— The presence of CH<sub>3</sub>CN along the outflow raises the question of whether the dust lanes are actually probing warm dust heated by the outflows (e.g., by shocks), rather than accretion filaments. There are, however, at least three counterarguments to this scenario. First, in W51e2e, there are at least four dust lanes with similar sizes and brightnesses, which appear elongated in several random directions relative to the SiO outflows (especially when considering we see a 2D projection from a 3D structure); therefore, it is unlikely that they all identify dust in the outflow cavities. Similar arguments apply to W51north, where there are three different lanes with no common point of symmetry. Second, if the outflow were responsible for the observed dust emission, the lack of bright emission toward the blueshifted lobe in the SE from W51e2e would imply a much lower density of material in that direction, yet the blue lobe truncates sharply at a distance of about 2000 au at a point where no hot dust emission is observed. The hot dust emission is therefore almost certainly driven by (1) the presence of (much) more gas+dust toward the NW than the SE and (2) the proximity of that gas+dust to the central star. Even if the outflow is interacting with this material, it is clear that there is a major asymmetry in the total mass. Third, we suspect that heated dust in an outflow cavity would be too weak to be seen at the distance of W51, while the measured high surface brightness along the filaments indicates a high intrinsic temperature.

Since these features are not part of an outflow, we suggest that they are accretion filaments feeding those central sources. Indirect evidence for infall comes from the fact that these dust lanes have a symmetric structure around protostellar sources with very high accretion rates (see Section 4.3). More indirect evidence comes from a previously published magnetic field study with ALMA, as we detail in the next paragraph.

Magnetic fields and filamentary accretion.—The magnetic field and gravity are the two main forces that influence the dynamics of dense cores where star formation takes place. We compare our observations with the polarization maps of Koch et al. (2018), who conducted a multiscale analysis of magnetic fields in W51. The plane-of-the-sky component of the magnetic fields inferred from the polarized dust emission exhibits a different morphology at angular resolutions of 2", 0", and 0"26 for W51e2e, W51e8, and W51north, respectively (see Figure 2 in Koch et al. 2018). At a resolution of 2'', the magnetic field in W51e2e displays a nearly uniform distribution in the east-west direction. The higher-resolution images reveal a radial distribution of the field centered at W51e2e. The magnetic field orientations align well with the major axes of the streamers presented in Figure 1. The alignment of the dust filaments with the radially distributed magnetic fields within the W51e2e core supports a scenario where the core collapse leads to accretion flows along the filaments that drag the magnetic fields, rending a radial distribution of the field lines. The dust emission toward the W51e8 and W51north cores is less filamentary compared to the W51e2e core. Nevertheless, the magnetic field maps in these two cores also exhibit radial



distributions that are suggestive of the field being dragged by the mass inflow. This scenario has been proposed to explain magnetic field properties in dust polarization studies of high-and low-mass star formation (e.g., Zhang et al. 2014; Hull & Zhang 2019; see also Section 5). Future observations of kinematics in the W51 cores are needed to confirm the accretion flows in these regions.

## 4.2. Upper Limits to Protostellar Disk Sizes

The compact cores at the centers of the dusty streamers (i.e., toward the dust continuum peaks) are where one would expect to see kinematic signatures of rotation (e.g., velocity gradients) if large accretion disks were present. Although we cannot directly estimate their actual size, we can measure upper limits on the potentially disk-containing regions based on the

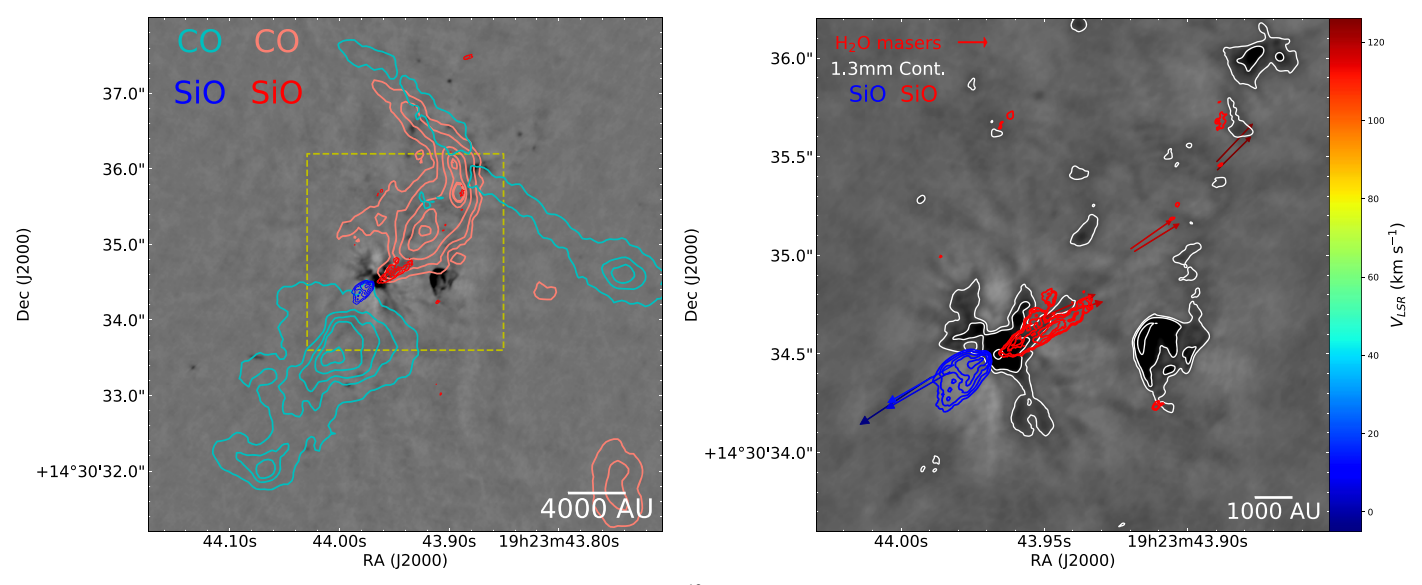


Figure 5. Outflow from W51e2e. In the left panel, the outflow is traced by the  $^{12}$ CO J=2-1 line from ALMA cycle 2 (beam size 0."2) and SiO J=5-4 line from ALMA cycle 3 (beam size 0."035). The CO emission is integrated over [0, 45] and [73, 180] km s<sup>-1</sup> for the blueshifted (cyan contours) and redshifted (salmon contours) emission, respectively. The SiO emission is integrated over [-56, 53] and [71, 159] km s<sup>-1</sup> for the blueshifted (blue contours) and redshifted (red contours) emission, respectively. These correspond to  $V_{\text{outflow}} = [-112, -3]$  and [15, 103] km s<sup>-1</sup> for  $V_{\text{sys}} = 56$  km s<sup>-1</sup>. The yellow dashed rectangle indicates the zoomed region plotted in the right panel. In the right panel, the outflow is traced by SiO emission and  $H_2$ O masers. The  $H_2$ O maser 3D velocities measured with the VLBA (Sato et al. 2010) are overplotted onto the total intensity of the redshifted (red contours) and blueshifted (blue contours) emission of the SiO J=5-4 line and the  $\lambda$ 1.3 mm continuum emission (white contours and gray-scale image). Colors denote maser line-of-sight velocity (color scales on the right-hand side). The blueshifted and redshifted water masers closer to the protostar imply a flow P.A. of  $-56^{\circ}$ , perfectly consistent with thermal SiO, while the redshifted masers along the outflow at larger distances have a P.A. of  $-43^{\circ}$ , closer to the  $^{12}$ CO outflow axis away from the protostar.

observed extent of the optically thick dust emission (Section 3.1.1). This yields diameters of 150 au for W51e8, 700 au for W51north, and 1000 au for W51e2e (indicated with black arrows in Figure 1).

The putative compact disks are surrounded by a morphologically flattened envelope of size of order of 1000-2000 au, where the filaments appear to converge. Zapata et al. (2009, 2010) used the SMA to reveal a large rotating structure on scales  $\gtrsim 10,000$  au. Although the maximum recovery scale in our study is only 0.4, which prevents us from recovering the large scales probed with the SMA, no such large-scale rotation was identified in the cycle 2 study with a maximum recovery scale of 9 (Ginsburg et al. 2017, Figures 31 and 32).

## 4.3. Outflow and Accretion Rate

Despite the lack of (large) disks, the presence of fast  $(\sim \pm 100 \text{ km s}^{-1})$ , collimated bipolar outflows in SiO emission provides a clear indication of ongoing accretion onto the three HMYSOs. Lacking a clear signature of accretion, we cannot directly estimate the mass accretion rate. In jet-protostar systems, however, ejection rates are expected to correlate with accretion/infall rates. Therefore, we can use the ejection rates calculated in Section 3.4 as a proxy for the infall/accretion rates. Here we use the term "infall rate" to describe gas in the core infalling onto the disk/protostar system and the term "accretion rate" to describe gas accreting onto the protostar itself. Therefore, we can define  $\dot{M}_{\rm infall} = \dot{M}_{\rm ejection} + \dot{M}_{\rm accretion}$ (assuming that the fraction of the infalling gas that is not accreted is actually reejected via protostellar winds/jets; e.g., Frank et al. 2014). We define  $f_j = \dot{M}_{\rm ejection} / \dot{M}_{\rm accretion}$  as the fraction of accreting gas that is launched in the jet. Therefore,  $\dot{M}_{\rm infall} = (1 + f_i)/f_i \times \dot{M}_{\rm ejection}$ . This fraction is observationally uncertain, but models predict  $f_i = 0.2-0.5$  (e.g., Offner & Arce 2014; Kuiper et al. 2016). Adopting these values implies  $\dot{M}_{\rm infall} \sim 3$ –6  $\dot{M}_{\rm ejection}$  and  $\dot{M}_{\rm accretion} \sim 2$ –5  $\dot{M}_{\rm ejection}$ . Using these assumed fractions, we infer infall rates of  $(2.6-5.2) \times 10^{-3}$  and  $(1.4-2.9) \times 10^{-3} \, M_{\odot} \, {\rm yr}^{-1}$  and accretion rates of  $(1.7-4.3) \times 10^{-3} \, {\rm and} \, (1.0-2.4) \times 10^{-3} \, M_{\odot} \, {\rm yr}^{-1}$  onto the W51e2e and W51north protostars, respectively.

## 4.4. Outflow from W51north: A Single Outflow Changing Direction on the Sky

In Section 3.3, we show that the W51north outflow appears to have changed direction substantially, as measured with a change of P.A. (projected onto the plane of the sky) from  $\sim -10^{\circ}$  to  $\sim -70^{\circ}$  from scales  $\gtrsim 2000-20,000$  au down to the smallest scales,  $\leq 200-1000$  au. Here we argue that this "multicomponent" morphological structure is best explained as a single protostellar outflow that has changed direction over a short period of time (but see possible alternative scenarios in Section 4.4.1). In this scenario, the prominent and compact SE-NW (P.A.  $\sim -70^{\circ}$ ) faster component represents the recently launched outflow, while the faint and diffuse north-south  $(P.A. \sim -10^{\circ})$  slower component represents a fossil outflow. In particular, assuming the outflow was driven at a constant velocity  $v_{\text{outflow}} = 30 \text{ km s}^{-1}$  (the average velocity of the bulk of the SiO emission), we infer the following history of the outflow.

1. "Old" flow. From about 22,000 to 1900 au, as traced by CO (and from about 4300, as traced by SiO), the outflow was consistently pointed at a P.A. of  $-13^{\circ}$  (3500–300 yr ago).

 $<sup>\</sup>overline{^{10}}$  The outflow in W51e8 appears to be nearly in the plane of the sky, making estimates of the infall/accretion rates less reliable.

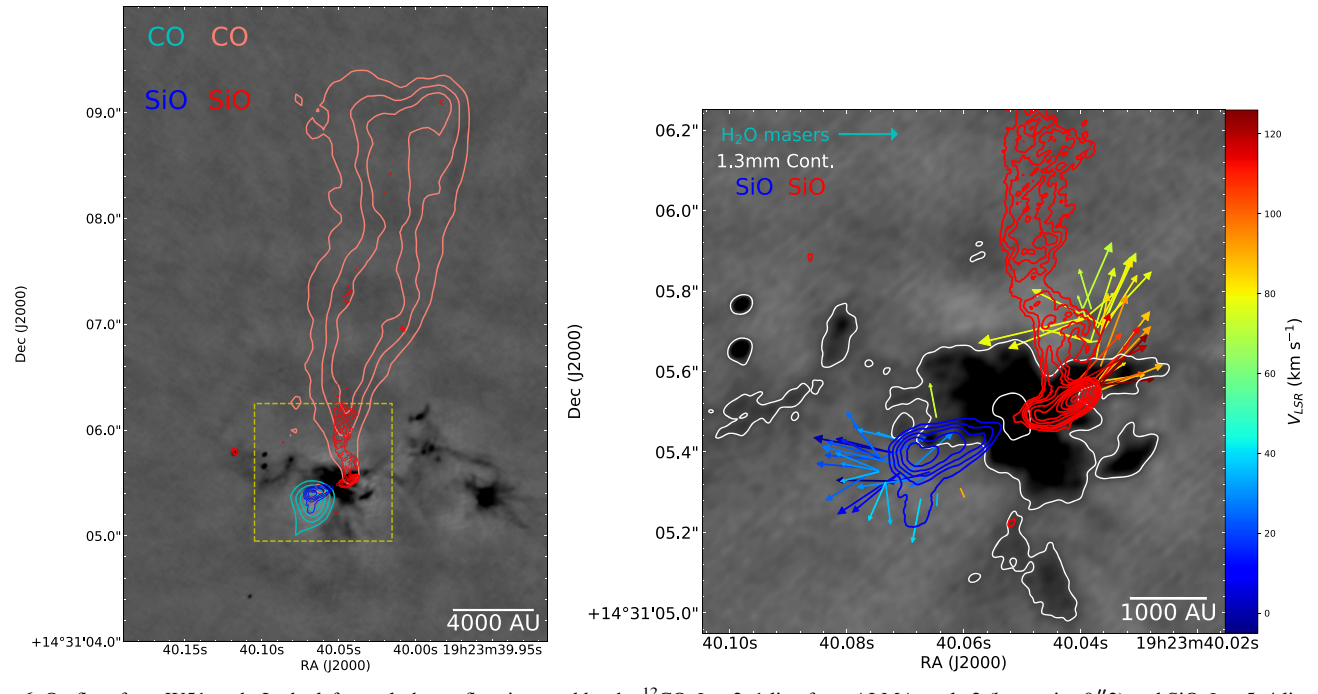


Figure 6. Outflow from W51north. In the left panel, the outflow is traced by the  $^{12}\text{CO}\ J = 2-1$  line from ALMA cycle 2 (beam size 0."2) and SiO J = 5-4 line from ALMA cycle 3 (beam size 0."035). The SiO emission is integrated over [-36, 56] and [66, 126] km s<sup>-1</sup> for the blueshifted (blue contours) and redshifted (red contours) emission, respectively. These correspond to  $V_{\text{outflow}} = [-96, -4]$  and [6, 66] km s<sup>-1</sup> for  $V_{\text{sys}} = 60$  km s<sup>-1</sup>. The yellow dashed rectangle indicates the zoomed region plotted in the right panel. In the right panel, the outflow is traced by SiO emission and H<sub>2</sub>O masers. The H<sub>2</sub>O maser 3D velocities measured with the VLBA (Imai et al. 2002) are overplotted onto the total intensity of the redshifted (red contours) and blueshifted (blue contours) emission of the SiO J = 5-4 line and the  $\lambda$ 1.3 mm continuum emission (white contours and gray-scale image). Colors denote maser line-of-sight velocity (color scales on the right-hand side). The H<sub>2</sub>O masers reside in two complexes separated by ~3000 au at the front edges of the compact SiO outflow lobes and are moving away from each other in ballistic motions at about 200 km s<sup>-1</sup> and at a P.A. of  $-72^{\circ}$ , consistent with the SiO NW–SE outflow.

- 2. "Transition" flow. From 1900 to 800 au, the outflow changes directions from a P.A. of  $-13^{\circ}$  to  $-70^{\circ}$  (300–125 yr ago, duration 175 yr).
- 3. "Young" flow. From 800 au to the resolution limit, the outflow has been consistently pointed along  $-70^{\circ}$  ( $\sim 125$  yr ago to now). This outflow history is sketched in Figure 7 for the SiO portion of the outflow. (See also Appendix C.1 for details on the dynamical age estimates.)

The outflow morphology fits this scenario; there is emission detected in both the red and blue lobes at intermediate P.A.s  $(-10^{\circ} > \text{P.A.} > -70^{\circ})$ . This emission is not as cleanly symmetric as the more linear "old" and "young" outflows, which may be caused either by asymmetries in the surrounding medium or by changing the speed of the outflow launch. A point in favor of this scenario is the lack of detected outflow emission in either SiO or CO (Ginsburg et al. 2017) beyond 1300 au along the current SE–NW outflow axis. If the W51north outflow has not changed direction in the last  $\sim$ 100 yr, the lack of observed outflow tracers at greater distances along the SE–NW implies that accretion onto this source only began in the last 100 yr. Given its high luminosity ( $L \gtrsim 10^4$   $L_{\odot}$ ), such an age is implausible.

The dramatic change of direction of the W51north outflow suggests a sudden major event that redirected the driving jet over the course of just 150–200 yr. This, in turn, indicates a substantial change in the orientation of the outflow-launching region, i.e., the accretion disk, over that same timescale. The large change in angle ( $\gtrsim 60^{\circ}$ ) suggests that small perturbations or instabilities in the disk are inadequate. Given the presence of a substantial reservoir of surrounding material distributed

asymmetrically around the source, we argue that accretion onto the disk is a likely cause for the change of outflow direction. Under the assumption that the present (young) outflow is the result of a single major accretion event and that the infall rate remained constant over the transition period (175 yr), from the infall rate estimated in Section 4.3, we infer that a mass of about 0.25– $0.5~M_{\odot}$  was dumped onto the protostar/disk system in such accretion event.

Is this mass enough to flip the disk? We assume that the disk has a radius of 350 au and a mass of 1  $M_{\odot}$  (i.e., a quarter of the compact core mass is in the disk; see Table 1) and is in Keplerian rotation about a 20  $M_{\odot}$  central star. The total angular momentum in such a disk would be  $L_{\rm disk} \sim 3 \times 10^{54} \, {\rm g \ cm^2 \ s^{-1}}$ (see calculation in Appendix D). If a 0.25–0.5  $M_{\odot}$  condensation impacts the disk at a radius of 350 au with a velocity of 10 km s<sup>-1</sup> (this corresponds to the infall velocity at 350 au toward a  $20 M_{\odot}$  star), the angular momentum of the impactor is  $L_{\rm dump} \sim (2.6-5.3) \times 10^{54} \sin \alpha \text{ g cm}^2 \text{ s}^{-1}$ , where  $\alpha$  is the angle between the impactor trajectory and the disk plane. For  $\alpha = 90^{\circ}$ , the disk angular momentum vector is reoriented by  $\theta = \tan^{-1}(L_{\text{dump}}/L_{\text{disk}}) = 41^{\circ}-61^{\circ}$  (for a smaller  $\alpha$ , the flip would be smaller by a factor  $\sin \alpha$ ). We explicitly notice that  $\theta$  is independent of the protostellar mass, since both  $L_{\text{dump}}$  and  $L_{\rm disk} \propto \sqrt{M_*}$ . We conclude that the accretion-driven disk reorientation model is plausible.

#### 4.4.1. Alternative Scenarios

We now consider alternative scenarios to explain the peculiar structure of the SiO outflow from W51north.

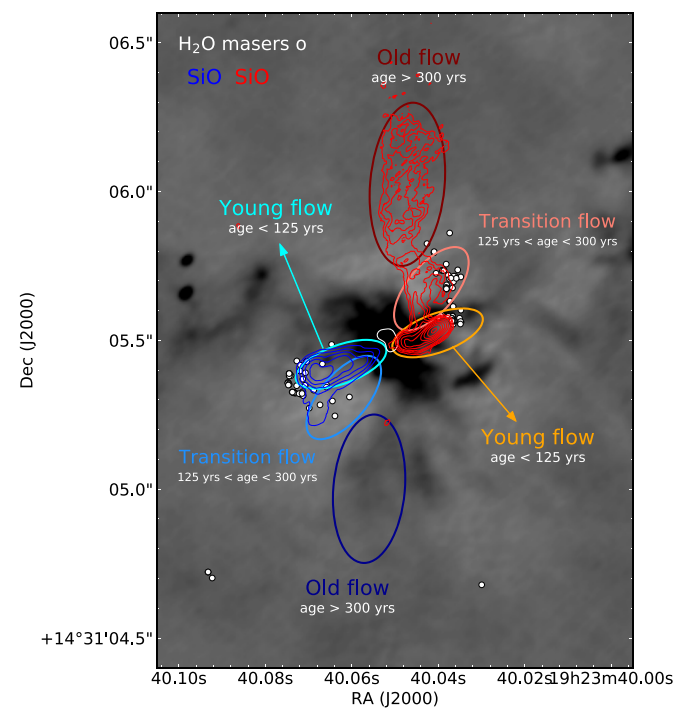


Figure 7. Sketch of the history of the outflow from W51north. The H<sub>2</sub>O maser positions (white circles) measured with the VLBA (Imai et al. 2002) are overplotted onto the total intensity of the redshifted (red contours) and blueshifted (blue contours) emission of the SiO J = 5–4 line and the  $\lambda 1.3$  mm continuum emission (gray-scale image). The colored ellipses identify three outflow components tracking its history: the "old" outflow (t > 300 yr) shows a fossil redshifted lobe (and a now-invisible blueshifted lobe) along the northsouth direction (indicated by the dark red and dark blue ellipses); the "young," bright outflow (t < 125 yr) is the present outflow with an axis along the SE-NW direction (indicated by the orange and cyan ellipses); and the "transition" flow (with a total duration of about 175 yr) represents material ejected while the outflow changes direction from PA  $-13^{\circ}$  to  $-70^{\circ}$  (identified by light red and light blue ellipses). The lack of the "old" blueshifted counterpart to the "old" redshifted lobe may be due either to some sort of localized blockage (so the outflow never blew out) or to the lack of material to be entrained (e.g., the outflow breaks out of the cloud). It is worth noting that even in the lowerresolution maps of the CO 2-1 emission, the blueshifted lobe is barely detected beyond about 0"30 or 1600 au (Ginsburg et al. 2017).

- 1. The outflow hits an "obstacle" in the surrounding dense clump and gets deflected in another direction (one jet-driving YSO).
- 2. There are two independent outflows driven by a binary with a separation <2000 au (two jet-driving YSOs).
- 3. There are three independent outflows driven by three different protostars within 2000 au (three jet-driving YSOs).
- 4. There is a single precessing outflow in a protostellar binary (one jet-driving YSO and one companion).
- A close stellar encounter (a flyby) changes the 3D orientation of the disk/jet system (one jet-driving YSO and one intruder).

Deflection by an obstacle.—This scenario requires the presence of two obstacles located at approximately the same distance from the central source along the axis of the outflow, and these obstacles must be angled such that the redshifted flow is deflected to the north and the blue flow to the south. Such a contrived scenario is implausible, since it requires a unique and unlikely set of conditions with no known analogs in the observational or theoretical literature.

Two independent outflows from a binary.—Two protostars in a binary, with a separation <2000 au and surrounded by two disks, would drive two independent outflows, seen on different spatial scales in CO and SiO line emission. Similar cases are known in the literature (e.g., the L1551 binary in the Taurus star-forming region; Rodríguez et al. 2003). In this case, we can rule out simultaneous independent outflows because we do not see high-velocity material close to the star in the north–south direction, implying that the north–south outflow is no longer there. The apparent continuity between the smaller NW–SE flow and the larger north–south flow is evidence against this hypothesis, since there is no reason these independent flows would be connected on large scales.

Three independent outflows driven by three different YSOs. -The powerful NE-SW outflow, the diffuse northern flow, and the faint southern flow could be driven by three independent YSOs. This scenario requires at least two undetected YSOs to be symmetrically offset from the central source and precisely at the locations of the intersections between the SiO and CO outflows. Each of these YSOs would have to drive a single-lobe outflow<sup>11</sup> in the blueshifted (south) and redshifted (north) directions. These single-lobe flows must also have velocities consistent with the brighter SiO outflow from the central source (redshifted for the northern YSO and blueshifted for the southern YSO). The detection of the W51north, e2e, and e8 outflows in SiO but nondetection of other SiO outflows in the field that contains dozens of candidate YSOs confirms that such high-brightness SiO outflows are very rare, so that even if there were two perfectly positioned YSOs, they are each unlikely to drive an SiO outflow. Combined, the various restrictions imposed by this scenario make it highly improbable.

Precessing outflow in a tight binary.—Theoretical models suggest that gravitational instabilities during the core collapse would cause the disk to fragment, resulting in massive binary or multiple systems, depending on the initial mass of the cloud (e.g., Krumholz et al. 2009). Tidal interactions between the disk associated with the primary and a companion star in a noncoplanar orbit would naturally lead to precession of the disk/jet system associated with the primary. Precessing outflows have been observed in massive binaries. Two wellknown examples are the two archetypal high-mass (B-type) YSO binaries IRAS 20126+4104 and Cepheus A. In both objects, there is evidence of steady precession over several thousand years possibly driven by a binary orbit that affects the disk (e.g., Cunningham et al. 2009). Qualitatively, the existence of these precessing outflows confirms that a singlesource outflow changing direction over time is possible. Although we cannot exclude the existence of a binary system at the center of W51north, the spatial and kinematic structure of the SiO/CO outflow is inconsistent with the expected jet precession.

We can use IRAS 20126+4104 as a benchmark to compare its observational properties to W51north. There are some significant structural and kinematical differences between the two sources. First, W51north does not show an S-shaped morphology on large scales (Shepherd et al. 2000; Cesaroni et al. 2005) or wiggling on small scales (Caratti o Garatti et al. 2008), as observed in IRAS 20126+4104, but rather displays

<sup>11</sup> Single-lobe outflows have been observed and can be explained with inclination effects and/or different densities of ambient material around the source.

two different outflow axes, one along the NW–SE direction (within 1600 au from the protostar) and one along the north–south direction (up to scales of 0.5 pc). This is inconsistent with a regular jet precession due to a binary and/or a multiple, but it is consistent with a sudden change of disk/outflow direction from a single YSO. Second, while in IRAS 20126+4104, the large-scale north–south outflow appears poorly collimated, as a consequence of the severe precession of the jet, in W51north, the two outflow components appear bipolar and collimated on both (small and large) scales. Third, in IRAS 20126+4104, the velocity of the lobes reverses so that the blueshifted gas is located to the SE at low velocities, whereas it appears to the NW at high velocities. In W51north, we do not see such a velocity reversal.

In summary, unlike IRAS 20126+4104 and Cepheus A, W51north exhibits a single shift in direction that occurred on a shorter timescale (when compared with the thousands or tens of thousands of years of their precessing jet), suggesting that a steady binary interaction is not the driver.

A stellar intruder hits the disk.—Since W51 is forming a dense protocluster (Ginsburg et al. 2016, 2017), it is likely that W51north formed in the presence of lower-mass protostars (see also discussion in the last paragraph of Section 5). If a close passage between a lower-mass protostar and W51north occurred about 150-200 vr ago, it is possible that the disk has been reoriented. Although we cannot rule out this scenario, the most probable effect of a close passage would be disk disruption (e.g., Moeckel & Goddi 2012), explosion-like events (e.g., Zapata et al. 2009; Bally et al. 2020), and/or stellar ejections (if more than two stars are involved; e.g., Goddi et al. 2011b; Rodríguez et al. 2020). The nicely collimated bipolar outflow on scales <1600 au, hinting at an an ordered disk, argues against this scenario. Even assuming that the disk would survive, the low collisional cross section between the disk and a star (whose effect is limited to the star's orbital radius, as opposed to gas inflow) would require several orbits, and therefore several close passages, to completely transfer its angular momentum to the disk/jet system. Given the short dynamical time of the outflow turn (<200 yr), this scenario is unlikely.

We conclude that the scenario where a single YSO changes its disk/jet orientation as a consequence of a substantial accretion event does not suffer from any of the improbability of the alternative scenarios considered here, and it is consistent with the observed morphology in several unique ways, therefore providing the best explanation for the W51north outflow.

## 5. General Implications for the High-mass Star Formation Process

The observational findings presented in this ALMA study support a scenario where accretion filaments are feeding compact (unsteady) disks, which drive collimated outflows that can change orientation over time. Such compact disks should also change their orientation, which implies loss of angular momentum support, probably due to varying angular momentum of the accreting material. The latter suggests episodic accretion and periods of (very) high accretion. Such a scenario has some interesting implications for our understanding of the high-mass star formation process, which we detail below.

Multidirectional unsteady accretion.—Modern 3D (M)HD simulations predict that accretion onto protostellar cores proceeds highly asymmetrically along filaments on scales greater than about 100 au (Commercon et al. 2011; Cunningham et al. 2011; Myers et al. 2013; Seifried et al. 2015; Rosen et al. 2016, 2019; Klassen et al. 2016; Rosen & Krumholz 2020).

For instance, Seifried et al. (2015) performed MHD simulations of turbulent and magnetized collapsing cores and showed that accretion of mass and angular momentum is highly anisotropic and proceeds through a few narrow and strongly pronounced channels on scales of order of 1000 au. These channels are reminiscent of the filamentary structure revealed by the dust continuum emission in our ALMA maps (e.g., compare their Figures 1 and 6 with the left panel of Figure 1). Rosen et al. (2016) added radiation feedback, and their 3D radiation-hydrodynamic simulations show that most of the mass is supplied to the accreting star via gravitational instabilities in dense filaments. Only when an extended disk is formed is the majority of mass delivered to the massive star via disk accretion. Similarly, Klassen et al. (2016) performed radiation-hydrodynamic simulations of collapsing protostellar cores with different initial masses (up to 200  $M_{\odot}$ ) and noticed that after a small protostellar disk starts forming (after 15 kyr), it becomes asymmetric and gravitationally unstable (after 25 kyr) and develops spiral density waves that act as accretion channels (with size of order 1000 au). Their simulations show steady inward gas motion across virtually all angles (besides accretion in the disk plane). They also find that the protostar launches powerful outflows with velocities exceeding 100  $km s^{-1}$ .

Our observations have achieved the angular resolution and sensitivity needed to identify these multidirectional accretion structures on scales of 100–2000 au and provide an experimental confirmation of the predictions of modern (M)HD simulations

Episodic accretion and transient disk/outflow systems.—A natural consequence of the multidirectional nature of the accretion flows is that the dominant angular momentum direction does not remain constant over the course of the mass assembly process (Smith et al. 2011; Rosen & Krumholz 2020). This, in turn, implies the occurrence of unsteady, episodic accretion events onto the disk and subsequently onto the protostar itself (Meyer et al. 2019). If the parent core feeding the central disk has a distribution of angular momentum vectors at different radii from the protostar, the central disk will accrete gas with time-dependent directions of the mean gas angular momentum vector. Irregular accretion may result in sudden changes of the orientation of the disk/jet when a large amount of material is suddenly accreted onto the disk. Since the disks reside at the center of larger-scale filaments, the buildup of a steady protostellar disk can occur only during periods when the accreting filaments do not significantly change their orientation relative to the disk. In W51north, a dramatic structural change in the orientation of the accretion channels and/or a large accretion event may have resulted in a sudden change of orientation of the accretion disk.

In the low-mass regime, evidence of episodic accretion is observed in FU Ori objects (e.g., Hartmann & Kenyon 1996; Audard et al. 2014), which exhibit sudden increases in the accretion rates (and therefore luminosities) of a few orders of magnitude that last from a few tens of years to a few centuries. Recently, a few outbursts in the high-mass regime have also

been reported in the literature. These events are marked by substantial increases in maser (Moscadelli et al. 2017) and dust emission at both millimeter (Hunter et al. 2017) and/or IR (Caratti o Garatti et al. 2017) wavelengths.

The rapid and substantial change in the disk orientation observed in W51north provides indirect observational evidence of a significant recent accretion burst in the growth of a massive protostar.

Magnetic fields and filamentary accretion.—In a survey of 14 high-mass star-forming regions with the SMA, Zhang et al. (2014) found that magnetic fields in 0.1 pc cores tend to be aligned with the field in the parsec-scale parental clump. Based on this statistical study, they concluded that the magnetic field is dynamically important during the fragmentation of the clump and the formation of dense cores. In addition, they found that the major axis of protostellar outflows does not appear to correlate with the magnetic field orientation in dense cores, which suggests that gravity and angular momentum may dominate the magnetic field from 0.1 pc core scales to the 100 au disk scale (see also Hull & Zhang 2019, for a review). The alignment of the dusty streamers with the radial magnetic field orientations within the W51e2e core (and to some extent in the W51e8 and W51north cores) is consistent with the findings in Zhang et al. (2014) and suggests a scenario where accretion flows along the filaments drag the magnetic fields, as suggested in Section 4.1.

Compact accretion disks.—Even with an unprecedented angular resolution of 20 mas, we do not identify disks in our protostellar sources, mainly because of the high optical depth of the dust continuum emission. Nevertheless, we believe disks are present based on collimated SiO outflows, and we estimate upper limits on the disk radii of <75 au for W51e8, 350 au for W51north, and 500 au for W51e2e. These upper limits are consistent with predictions from recent (M)HD simulations. In particular, simulations producing asymmetric accretion flows suggest that the disks should only form on scales less than about 100 au (Commercon et al. 2011; Seifried et al. 2012, 2013, 2015; Myers et al. 2013), whereas simulations that have more ordered initial conditions and do not produce asymmetric flows (Krumholz et al. 2009; Kuiper et al. 2011; Klassen et al. 2016) often produce much larger (~500–1000 au) disks.

We can now compare the disk size upper limits derived in this study with the existing measurements of disks in other HMYSOs. In Table 3 in Appendix E, we list all known Keplerian disk candidates around HMYSOs based on ALMA observations to date. The majority of disks have radii in the range 300–1000 au. Most of these disks would be resolved in this ALMA long-baseline data set at  $d_{\rm W51}=5.4\,{\rm kpc}$ ; only the smallest few would be missed.

So why are the disks larger in other HMYSOs? —In an attempt to address this question, in the following, we will explore two additional star formation properties: evolution and environment.

Evolutionary stage and disk detection rate.—The lack of large disks in W51, as well as the low disk detection rate around HMYSOs, could be related to their evolutionary stage. Cesaroni et al. (2017) explored the properties of seven HMYSOs hosting rotation disk candidates using ALMA at 0."2 resolution. In particular, they plotted the luminosity-to-gas mass ratio (an evolutionary stage indicator) as a function of the distance for all seven HMYSOs and concluded that the disk detection rate could be sensitive to protostellar evolution. In particular, in young,

deeply embedded sources, the evidence for (Keplerian) disks could be weak because of confusion with the surrounding infalling envelope or toroid (e.g., G351.77-0.54; Beuther et al. 2017), while in the most evolved sources, the molecular component of the disk could have already been greatly reduced or completely dispersed, resulting in either very small disks with r < 50-100 au (e.g., Orion source I, Ginsburg et al. 2018; and G17.64+0.16, Maud et al. 2019) or no disk at all. Only in those objects that are at an intermediate stage of the evolution could the molecular gas emission reveal the presence of an underlying disk. This evolutionary trend is supported by the numerical simulations cited above, which predict that Keplerian disks are constantly being fed material from large-scale infalling filaments and grow with time from the inside out, from tens of au up to  $\sim$ 1000 au (e.g., Kuiper et al. 2011; Klassen et al. 2016; Rosen et al. 2016).

Evolutionary stage and ionization rate.—One typical indicator of evolution in high-mass star formation is provided by radio continuum emission produced by photoionization induced by Lyman photons. When the HMYSOs reach the zero-age main sequence, they produce copious amounts of ultraviolet radiation and start ionizing their surroundings, forming compact H II regions. The HMYSOs can also exhibit radio continuum via shock ionization in jets/outflows (e.g., Moscadelli et al. 2016; Sanna et al. 2018). The HMYSOs listed in Table 3 are all known to exhibit radio continuum emission, in the form of either an ionized wind/jet or a compact H II region, indicating that they are relatively evolved. 12 The nondetection of radio continuum emission, and in particular the lack of an observable HII region, toward the three HMYSOs studied here suggests that they may still be in the pre-main sequence and can therefore be considered the high-mass counterparts to the "class 0" stage in solar-like stars. This could explain why we do not see large disks.

Evolutionary stage and high accretion rate.—In the alternative, the nondetection of radio continuum emission could be a consequence of very high density accretion flows. In fact, detailed theoretical studies suggest that the evolution of a highmass protostar depends strongly on the accretion rate onto the protostellar surface and the exact accretion geometry (Keto 2003; Hosokawa et al. 2010). For example, a high accretion rate ( $\geq 10^3$  $M_{\odot} \text{ yr}^{-1}$ ), as inferred for the three HMYSOs in W51 (and generally expected for high-mass star formation; e.g., Zinnecker & Yorke 2007), could result in a quenched or trapped H II region (Keto 2003; Keto & Wood 2006). This scenario, however, requires spherical symmetry and is therefore disfavored by our data, which show highly asymmetric accretion flows. In the alternative, high accretion rates can change the properties of the underlying star, bloating it and reducing its effective photospheric temperature (Hosokawa & Omukai 2009; Smith et al. 2012; Hosokawa et al. 2016; Tanaka et al. 2016). This significantly delays stellar ignition (up to  $20 M_{\odot}$ ), changing the history of the energy feedback (e.g., bolometric luminosity, total amount of Lyman photons, etc.). Therefore, the lack of an observable HII region could actually be explained with high accretion rates in a bloated HMYSO. We explicitly note that this mechanism has been proposed to explain the low luminosity  $(\sim 10^4 L_{\odot})$  estimated for G11.92–0.61 MM1, which, with a mass of  $34 \pm 5 M_{\odot}$  (Ilee et al. 2018), is the most massive O-type

<sup>&</sup>lt;sup>12</sup>An exception is G351.77–0.54 because, to the best of our knowledge, it does not produce radio continuum emission.

Keplerian disk candidate known to date (see Table 3 in Appendix E).

Protostellar disk evolution and protocluster environment.— A final question worth addressing is whether the two properties of the disks we have unveiled (small size and changing orientation) are intrinsic to the high-mass star formation evolution or due to the dense cluster environment. On parsec scales, W51 contains tenfold more mass than other nearby regions (e.g., Ginsburg et al. 2016, 2017), and, assuming a standard star formation conversion rate, we would expect to form 10 times more stars relative to a typical 1000  $M_{\odot}$  pc<sup>-1</sup> scale clump (Ginsburg et al. 2013). So the three HMYSOs studied here are likely forming in the presence of lower-mass condensations and/or lower-mass stars that could have been interacting with them. Simulations of such clustered environments find that boosting of the accretion rate can be induced with protostellar encounters (Pfalzner 2008) or even mergers (Bonnell & Bate 2005). It is an open question whether the dense stellar environment is affecting the protostellar (disk) evolution on the scales resolved in this study, i.e., 100–2000 au (Rosen et al. 2016, 2019).

## 6. Summary and Conclusions

Using the ALMA longest baselines (16 km) at 1.3 mm (Band 6), we have mapped the innermost regions around three deeply embedded high-mass protostars belonging to the W51 star-forming complex with very high spatial resolution (~100–200 au).

We summarize the main findings of this study as follows.

- 1. The high angular resolution (~0."03 beam size) ALMA maps of the dust continuum emission reveal complex filamentary structures that are ~2000 au long and converge onto compact cores. No clear kinematic information can be extracted toward these filaments or the compact cores, most likely because of high optical depth in the dust continuum.
- 2. The central sources in the cores drive young ( $\sim$ 100 yr), compact ( $\lesssim$ 2000 au), fast ( $\sim$ 100 km s<sup>-1</sup>), collimated SiO outflows. From outflow ejection rates, we infer accretion rates of (1.7–4.3)  $\times$  10<sup>-3</sup> and (1.0–2.4)  $\times$  10<sup>-3</sup>  $M_{\odot}$  yr<sup>-1</sup> onto the W51e2e and W51north protostars, respectively, indicating that they are vigorously accreting.
- 3. We measure upper limits on the disk radii of <75 au for W51e8, 350 au for W51north, and 500 au for W51e2e.
- 4. The outflow from W51north displays a multicomponent morphological structure. We argue that this structure is best explained as a single protostellar outflow that has changed direction over a short period of time as a consequence of a substantial accretion event onto its disk.

The accretion/outflow structures observed in the W51 HMYSOs appear much more complex than generally observed in class 0 protostars (but see, for instance, Tobin et al. 2012, for examples of complex structures in class 0 envelopes). Their properties are also different from those inferred from Keplerian-like disks recently reported around OB-type HMY-SOs (see Table 3 in Appendix E), which generally appear to be at a later evolutionary stage and are forming in less dense, clustered environments.

In order to interpret the observed circumstellar structures, we propose the following scenario.

- 1. The observed small-scale dusty streamers are imprints of accretion columns toward the central HMYSOs. While there are no kinematic data to confirm this hypothesis, it is the simplest explanation consistent with both the continuum structure and the high outflow rates.
- These accretion channels inhibit the formation of large, steady disks (at least in the early stage of formation) but feed central compact disks, whose presence is inferred from the existence of massive and powerful bipolar outflows.
- 3. These compact disks are not the classic smooth, steady disks seen around low-mass stars and in rotating core simulations but instead are truncated and change orientation over time, as seen in more turbulent simulations.
- 4. Outflows changing direction mark the occurrence of unsteady, episodic accretion events onto the disk and subsequently onto the protostar itself, leading to accretion and luminosity bursts (Meyer et al. 2017, 2019).

When put together, these findings contrast with a simplified vision of an ordered disk/jet geometry and point to a different type of accretion that we call "multidirectional accretion," where the accreting material has a different angular momentum vector over time.

Further high-resolution observations at lower frequencies with ALMA or in the future with the ngVLA are required to elucidate the nature of the dusty streamers and identify disks in the central cores by unveiling their dynamics. Similar studies targeting the most massive hot cores known in the Galaxy would allow us to assess whether this multidirectional accretion mode is the standard route for the formation of the most massive stars in dense stellar environments.

This paper makes use of the following ALMA data: 2013.1.00308.S and 2015.1.01596.S. ALMA is a partnership of the ESO (representing its member states), NSF (USA), and NINS (Japan), together with the NRC (Canada), NSC and ASIAA (Taiwan), and KASI (Republic of Korea), in cooperation with the Republic of Chile. The Joint ALMA Observatory is operated by the ESO, AUI/NRAO, and NAOJ. C.G., as the PI of ALMA project 2015.1.01596.S, acknowledges assistance from Allegro, the European ALMA Regional Center node in the Netherlands. C.G. acknowledges financial support from ERC synergy grant 610058. L.A.Z. acknowledges financial support from CONACyT-280775 and UNAM-PAPIIT IN110618 grants, Mexico. A.G. acknowledges support from the National Science Foundation under grant No. 2008101.

## Appendix A Why Do We Not See Kinematical Signatures of Accretion?

We have looked for the expected signatures of accretion onto a high-mass, high-luminosity protostar embedded in a core that is optically thick in the continuum, in particular, (a) higher-excitation lines should be redshifted compared to lower-excitation lines (warmer gas should be moving with higher velocities toward the center) and (b) the spectral profiles should be moderately asymmetric (skewed toward the blueshifted component; e.g., Goddi et al. 2016). However, the velocity field appears to be approximately flat across the core for the three sources. While some lines show some signs of different velocity absorption features, these are all low-excitation lines

(e.g.,  $^{13}$ CO,  $H_2$ CO) that demonstrably trace the broader molecular cloud, not the core.

If there are genuinely massive, accreting cores in these objects, as demonstrated by the presence of powerful outflows, some infall must be occurring. A few solutions are possible for its nondetection.

- 1. All gas is accreting in the plane of the sky. Since we see three sources, none of which have clear kinematic accretion signatures and all of which have detectable outflow kinematic signatures, this possibility is implausible.
- 2. Radiative transfer effects are hiding the kinematic signatures. In low-mass cores, (double-peaked) symmetric line profiles are expected in optically thin tracers and inverse P Cygni profiles in optically thick lines. However, in low-mass cores, the continuum is almost always optically thin and has a relatively low brightness temperature. In the high-mass cores we observe, the continuum brightness temperature is very high, leading us to infer that the optical depth is similarly high. As we probe closer to the star (where the velocities are expected to be higher), the gas temperature rises and approaches equilibrium with the dust. If  $T_{\rm gas} = T_{\rm dust}$ , as  $\tau_{\rm dust} \to 1$ , any absorption signature from the molecular line approaches zero. This means we should not expect to see the highest velocities in absorption at all, but we should see very strong absorption from cooler gas further in front of the core. The point at which we begin to detect molecular absorption indicates the approximate location of the  $\tau_{\text{dust}} = 1$  surface, but it is not a very strong probe, since what we observe is a mass-weighted profile of the foreground gas. This mechanism readily explains the lack of signatures in the absorption lines toward each source.
- 3. A purely observational effect hides the emission. When lines appear as absorption features toward the continuum source and emission features off of the source, the average surface brightness in a given velocity channel approaches a smooth, constant value. Because we are observing with an interferometer with a low spatial dynamic range, these smoother features are suppressed. It is likely that this effect is sufficient to push any emission signatures below the noise of our current data set.

We regard explanation (2) above as the most relevant. It implies that longer-wavelength observations, where the dust may be optically thin, are necessary to detect infall kinematics and measure the dynamical masses of high-mass protostars. We note that our finding that the dust opacity prevents kinematic measurements on small scales in high-mass protostellar disks using dense gas molecular lines was explicitly predicted in Krumholz et al. (2007).

## Appendix B Spatial and Velocity Structure of Outflows

Here we complement high angular resolution images of the thermal SiO J=5–4 line from ALMA cycle 3 (beam size 0."035) with lower-resolution images of  $^{12}$ CO J=2–1 from ALMA cycle 2 (beam size 0."2), as well as Very Long Baseline Array (VLBA) measurements of  $H_2$ O masers (beam size 0."001). We focus on W51e2e and W51north because their outflows display complex spatial and velocity structures (we were unable to trace the larger-scale outflow from W51e8). The combination of different tracers provides us with a full picture

of these outflows on scales ranging from hundreds to tens of thousands of au.

### B.1. W51e2e

A prominent bipolar outflow, which was first detected in the CO (3-2) line with the SMA by Shi et al. (2010b) and then imaged with ALMA in the CO (2–1) line at 0"2 resolution by Ginsburg et al. (2017; Figure 5, left panel), is driven by W51e2e. This outflow has a high relative velocity,  $v \pm 100 \text{ km s}^{-1}$ . On the largest scales traced by <sup>12</sup>CO, both ends (red- and blueshifted) of the outflow are sharply truncated at  $\sim 2.75$  (0.07 pc or 15,000 au). To the southeast (SE), the high-velocity flow lies along a line that is consistent with the extrapolation from the NW flow (i.e., directly bipolar); however, at lower velocities (10 km s<sup>-1</sup>  $< V_{LSR} <$ 45 km s<sup>-1</sup>), the direction appears more to the south before being abruptly truncated. For the NW redshifted part of this outflow (70 km s<sup>-1</sup> <  $V_{\rm LSR}$  < 120 km s<sup>-1</sup>), there is apparently a clear bend at an intersection with a blueshifted flow (22 km s<sup>-</sup>  $< V_{\rm LSR} < 45~{\rm km~s^{-1}}$ ) from another source, W51e2nw, that is also believed to be an intermediate-to-high-mass protostar (Goddi et al. 2016). The significant change in direction suggests that these two outflows interact. Although such a scenario seems implausible given the outflows' small volume filling factor, both the morphology and the distinct velocity range of the two outflows (which make it easy to distinguish the two) point to a genuine encounter. Therefore, at least for the NW flow, this encounter is responsible for the truncation of the redshifted lobe.

The ALMA long-baseline images unveil the smallest scales of this outflow (Figure 5, right panel). Although the SiO structure is broadly consistent with the lower-resolution <sup>12</sup>CO structure at the base of the outflow, the P.A. of the line connecting the NW and SE flows is  $-56^{\circ}$  (whereas the  $^{12}CO$  outflow is closer to P.A. =  $-37^{\circ}$ ). The blueshifted flow extends only across  $\sim 0.45^{\circ}$ or 2430 au. The bulk emission of the redshifted lobe in the NW has a similarly compact size ( $\sim 0.6'$  or 3240 au), but some weaker emission extends across  $\sim$ 10,000 au and is cospatial with the <sup>12</sup>CO outflow (this more extended, weaker structure is recovered in lower-resolution images of SiO tapered to 0.11, not displayed here). Interestingly, the redshifted lobe shows a twostream limb-brightened morphology with a central cavity, possibly due to the presence of a dusty filament at the center (see left panel of Figure 1). The dynamical age of the SiO outflow is  $\sim$ 116 yr (see Appendix C.1), shorter than the 600 yr estimated by Ginsburg et al. (2017) at the peak observed velocity of <sup>12</sup>CO.

Sato et al. (2010) used the VLBA to measure proper motions of water masers, which also show a picture consistent with the thermal  $^{12}\text{CO}$  and SiO emission. Interestingly, the blueshifted and redshifted water masers closer to the protostar imply a flow P.A. of  $-56^{\circ}$ , perfectly consistent with thermal SiO, while the redshifted masers along the outflow at larger distances have a P.A. of  $-43^{\circ}$ , closer to that of the  $^{12}\text{CO}$  outflow axis spatially distant from the protostar. Considered together, these findings are consistent with an indication of a change in the P.A. of the outflow with increasing distance from the protostar.

## B.2. W51north

The outflow from W51north is remarkably extended and complex. Figure 6 offers a full view of this outflow on scales from 25,000 au down to hundreds of au. The first notable feature is that the redshifted and blueshifted lobes on the large scales as traced by <sup>12</sup>CO are significantly asymmetric. A collimated high-velocity

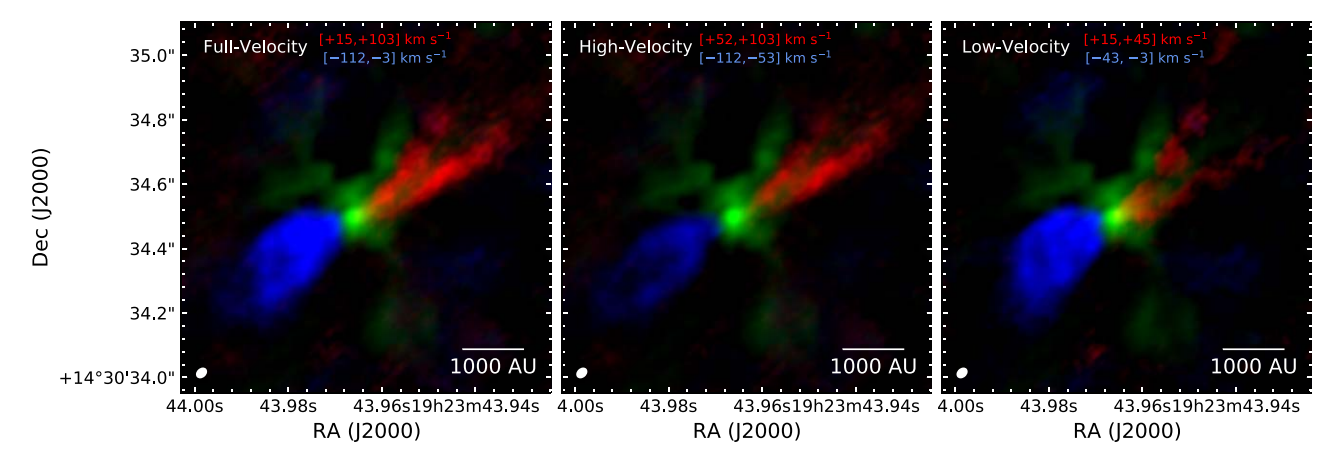


**Figure 8.** Structure of the massive protostellar outflow driven by W51e2e as a function of velocity within 3000 au from the central protostar. Red and blue indicate redshifted and blueshifted emission of the SiO J = 5–4 line. The emission is integrated over different velocity ranges (indicated in brackets at the top of each panel): full velocity range (left panel), high-velocity range (middle panel), and low-velocity range (right panel). The velocity ranges are with respect to the systemic velocity of the protostar (56 km s<sup>-1</sup>). Green displays the dust continuum emission at 1.3 mm, already shown in Figure 1 in the main text; here a different "stretch" of the intensity brightness (*arcsinh* function in the *matplotlib* Python plotting library) is employed to highlight the central core (and filter out the complex filamentary structure). The angular resolution of these data is given by the ellipse drawn in the lower left corner (same as Figure 1 in the main text).

component (covered velocities of  $\pm 100$  km s<sup>-1</sup>) extends directly north across  $\sim 4''$  (or 20,000 au), while the blueshifted component points to the SE and is sharply truncated, extending only across  $\sim 0.0''$ 6 (or 3200 au; Figure 6, left panel; Ginsburg et al. 2017). At the smallest scales, i.e., within a few thousand au from the driving source (Figure 6, right panel), further surprises are revealed. At the base of the <sup>12</sup>CO outflow, SiO reveals a very fast and well-collimated bipolar outflow, with the blue lobe extending across 0.0''34 (or 1600 au) and having a maximum speed of 96 km s<sup>-1</sup>. The red lobe is slightly more compact, with a radius of 0.0''24 or 1300 au and a maximum speed of 66 km s<sup>-1</sup>. Both SiO lobes are consistently oriented at P.A.  $\sim -70^\circ$ , clearly rotated from the large-scale <sup>12</sup>CO, which has a P.A. of  $-13^\circ$  (Figure 6, left panel).

Close to the central protostar, the redshifted outflow lobe shows a remarkable structure. It has an orientation consistent with that of the blueshifted lobe at P.A.  $\sim -70^{\circ}$ , up to a radius of 0."24 (1300 au). Starting at about 0."15 (800 au) from the center, it suddenly turns by  $80^{\circ}$  (P.A.  $\sim 10^{\circ}$ ) and curves until it settles at a P.A. of 0° along the base of the redshifted lobe of the <sup>12</sup>CO outflow. The high-velocity portions of the flow (up to  $\sim$ 70 km s<sup>-1</sup> from the systemic velocity) are found closer to the protostar, while the material in the "transition" region has a lower velocity (65 km s<sup>-1</sup>  $< V_{LSR} < 90$  km s<sup>-1</sup>, i.e., within 30 km s<sup>-1</sup> from the stellar systemic velocity). Some highvelocity material (up to 50 km s<sup>-1</sup> from the systemic velocity) is also observed at the northern end of the SiO emission (see Appendix B.3 and Figure 9 for a description of the velocity structure of the outflows). The large-scale red lobe shows contiguous structure tracing onto the small scale, with the change in direction starting at around 0."35 (1900 au) and completing by about 0."15 (800 au). Assuming a constant velocity of 30 km s<sup>-1</sup>, the outflow turn occurred over just 175 yr. The general structure, including the sharp turn seen in the redshifted lobe, is reflected in the blueshifted lobe, which shows a southward "protrusion" starting at about 0"22 (1200 au) from the protostar. Although much less prominent, this southern component in the blueshifted SiO lobe provides a (weaker and more compact) counterpart to the redshifted northern component. In both SiO and CO emission, the blueshifted lobe is barely detected beyond about 0"30 or

1600 au (although the weakest CO emission extends up to 3200 au); one possibility is that it breaks out of the cloud (assuming the source is located at the front of it).

The peculiar structure of the outflow revealed by ALMA images of SiO emission is also tracked by the H<sub>2</sub>O maser 3D velocities (Imai et al. 2002), shown as colored arrows in the right panel of Figure 6. The H<sub>2</sub>O masers reside in two complexes separated by  $\sim 3000$  au at the front edges of the compact SiO outflow lobes<sup>13</sup> and are moving away from each other in ballistic motions at about 200 km s<sup>-1</sup> and at a P.A. of  $-72^{\circ}$ , consistent in both P.A. and velocity with the SiO compact outflow. In particular, the H<sub>2</sub>O masers detected in the SE appear to trace a bow shock at the tip of the blueshifted SiO lobe, while the H<sub>2</sub>O maser complex on the opposite side traces both the high-velocity NW redshifted lobe and the base of the northern outflow component. In the redshifted part of the outflow, the measured proper motions appear to smoothly rotate from NW to north moving away from the tip of the SiO lobe, closely following the SiO emission. In addition, the expansion velocity of the H<sub>2</sub>O maser outflow decreases from 90 to 50 km s<sup>-1</sup> at radii 0."2-0."5 from the outflow origin, also consistent with the SiO redshifted emission. Finally, a leastsquares fitting analysis to the measured maser 3D motions provides evidence of a triaxial symmetry, inconsistent with a simple bipolar symmetric outflow but consistent with multiple outflows or a single outflow with a more complex structure.

### B.3. Velocity Structure as a Function of Distance

Figures 8 and 9 showcase the structure of the SiO protostellar outflows as a function of velocity within 3000 and 4000 au from the central protostars W51e2e and W51north, respectively. Note that in W51e2e, the high velocities preferentially trace the central parts (i.e., primary wind), and the low velocities preferentially trace the limb-brightened edges

 $<sup>\</sup>overline{^{13}}$  We registered the H<sub>2</sub>O maser positions and our ALMA maps under the assumption that the H<sub>2</sub>O maser outflow origin (estimated with a least-squares fitting analysis of the measured maser 3D motions; Imai et al. 2002) is coincident with the peak of the dust continuum and/or the origin of the SiO outflow imaged with ALMA. We assume that this is the putative location of the driving protostar.

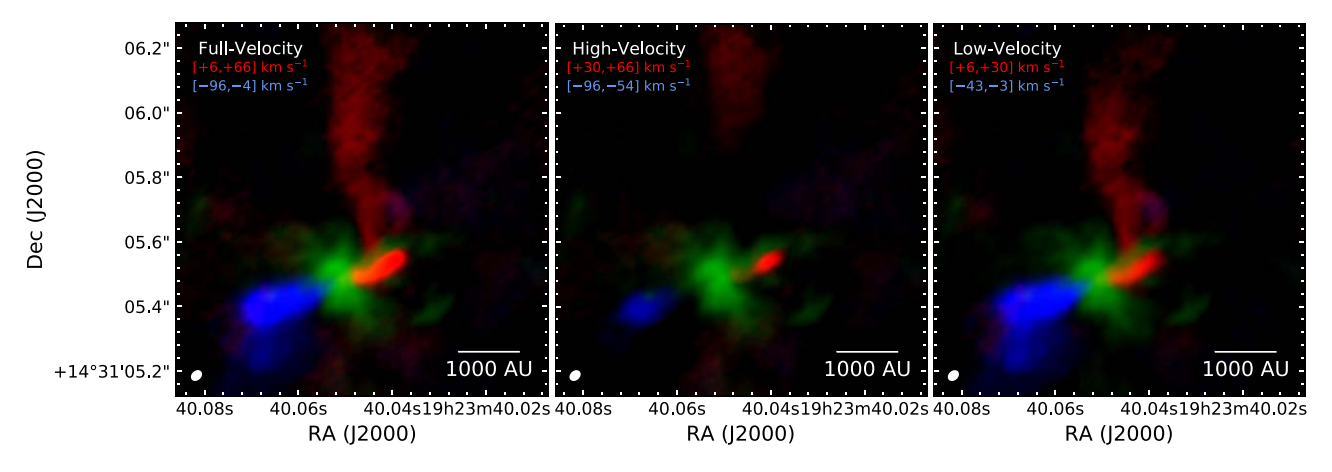


**Figure 9.** Structure of the massive protostellar outflow driven by W51north as a function of velocity within 4000 au from the central protostar. Red and blue indicate redshifted and blueshifted emission of the SiO J = 5–4 line. The emission is integrated over different velocity ranges (indicated in brackets in the upper left corner of each panel): full velocity range (left panel), high-velocity range (middle panel), and low-velocity range (right panel). The velocity ranges are with respect to the systemic velocity of the protostar (60 km s<sup>-1</sup>). Green displays the dust continuum emission at 1.3 mm, already shown in Figure 1 in the main text; here a different "stretch" of the intensity brightness (*arcsinh* function in the *matplotlib* Python plotting library) is employed to highlight the central core (and filter out the complex filamentary structure). The angular resolution of these data is given by the ellipse drawn in the lower left corner (same as Figure 1 in the main text).

(i.e., entrained gas) of the outflow, a phenomenon often observed in low-mass protostellar outflows (Frank et al. 2014). In W51north, the high velocities trace material at larger radii from the protostar both in the compact NW–SE outflow and the larger-scale north–south outflow, reminiscent of the "Hubble flows" observed in low-mass protostellar outflows. It is also interesting to note that the bulk of the compact NW–SE outflow expands at high velocities, while the bulk of the larger-scale north–south outflow expands at low velocities, in agreement with the scenario where the former represents the latest outflow event and the latter is a fossil outflow.

## Appendix C Physical Properties of Massive Protostellar Outflows

## C.1. Dynamical Ages

To estimate the dynamical age of the outflows,  $T_{\rm dyn}$ , we take the ratio of the projected length (measured from the protostar),  $R_{\rm max}$ , to the the maximum speed of the outflow,  $V_{\rm max}$ , corrected for the inclination i:  $T_{\rm dyn}(V_{\rm max}) = (R_{\rm max}/V_{\rm max})/\tan(i)$ .

Toward W51e2e, the outflow is clearly bipolar and fairly symmetric, though the redshifted side is partly obscured by the dust continuum; therefore, we use the blue lobe in our estimates. We observe a maximum velocity of 105 km s<sup>-1</sup> ( $v_{\rm LSR} = -50~{\rm km~s^{-1}}$ ) at a separation of about 2560 au, which gives a dynamical age  $T_{\rm dyn}(V_{\rm max}) = 116 \times ({\rm tan}(45^{\circ})/{\rm tan}(i))$  yr, where the inclination i is expressed in units of degrees.

In W51e8, the highest observed outflow velocity is 42 km s<sup>-1</sup> at a separation of about 390 au, which corresponds to  $T_{\rm dyn}(V_{\rm max}) = 44/\tan(i/45^\circ)$  yr. However, we warn the reader that the outflow appears to be nearly in the plane of the sky; therefore, the age estimate is not reliable.

In W51north, we first consider the blueshifted lobe, which displays a much simpler structure. We observe a maximum velocity of 95 km s<sup>-1</sup> ( $v_{LSR} = -35 \text{ km s}^{-1}$ ) at a separation of about 1540 au, which gives a dynamical age  $T_{\rm dyn}(V_{\rm max}) = 77 \times (\tan(45^\circ)/\tan(i))$  yr.

The redshifted lobe from W51north breaks into three major components, representing three consecutive events; these are labeled as "young," "transition," and "old" in Figure 7. The "young" flow is the component along the NW-SE close to the protostar. For a maximum velocity of 66 km s<sup>-1</sup> at a separation of about 1300 au, the dynamical age is  $\sim 100 \times (\tan(45^{\circ}) / \tan(i))$ yr, higher than inferred from the blueshifted lobe. Adopting an average velocity of  $\sim 30 \text{ km s}^{-1}$  at a separation of 800 au (where the second component starts), one gets 125 yr. The second component, which identifies the "transition" between the young NW–SE component and the old north–south component, extends from 800 to 1900 au, corresponding to 300-125 yr (or a duration of 175 yr) using an average velocity of 30 km s<sup>-1</sup>. The third component is the larger-scale "old" north-south outflow and extends up to 0.18 or about 4300 au, yielding an age of 680 yr for a 30 km s<sup>-1</sup> velocity. An even older component of the outflow is traced by <sup>12</sup>CO, up to a length of about 4" or 22000 au, corresponding to an age of about 3500 yr (for an average velocity of  $30 \,\mathrm{km \ s^{-1}}$ ).

## C.2. Momentum Rate

In order to determine the momentum of the outflowing gas, we compute its total mass from the SiO emission integrated in the full velocity range. We follow a standard approach in two steps.

As a first step, we measure the number of SiO molecules per unit area along the line of sight. We first calculate the column density of SiO in the energy level corresponding to the observed transition J=5-4 using the measured intensity of that transition (channel by channel) and the Boltzmann equation for statistical equilibrium coupled with the standard radiative transfer equation, e.g., the optically thin version of Equation (30) in Mangum & Shirley (2015). Then we relate the number of molecules in the given energy level to the total population of all energy levels in the molecule, assuming that they are populated according to a Boltzmann distribution; we use the rotational partition function, a quantity that represents a statistical sum over all rotational energy levels in the molecule, and we assume a constant temperature defined by the excitation

<sup>&</sup>lt;sup>14</sup> This method is adequate, since the highest speeds are observed at the largest separations (see Appendix B.3).

temperature  $T_{\rm ex}$ , e.g., Equation (31) in Mangum & Shirley (2015). We adopt  $T_{\rm ex} = 250$  K (note that the partition function is approximately linear with  $T_{\rm ex}$  in this regime, so if the molecules are twice as hot, the column estimate should be halved).

In the second step, we use the SiO column density to compute the total mass of the molecular gas. To convert from the SiO column to the H<sub>2</sub> column, we assume a conservatively high abundance of SiO:  $N(\text{SiO})/N(\text{H}_2) = 10^{-7}$ . The total momentum is then obtained by integrating over the full velocity range of SiO emission:  $P_a = \sum_{\nu} m_{\nu} \nu$ .

In our analysis, we treated the blueshifted and redshifted lobes independently, but the latter provided mass values 4–10 times lower. In fact, in W51e2e, the redshifted lobe is partly obscured by the dust continuum, whereas in W51north, the redshifted side shows a more complex structure than the blueshifted side, yielding more uncertain estimates. To mitigate these observational biases, we used the blue flows alone in our estimates. The outflow masses and momenta derived with this analysis are reported in columns 6 and 7 of Table 2. In order to account for both outflow lobes, we thus need to multiply those numbers by a factor of 2, yielding total masses of 0.36, 0.72, and  $0.22~M_{\odot}$  and total momenta of 18, 50, and  $3~M_{\odot}$  km s<sup>-1</sup> for the outflows driven by W51north, W51e2e, and W51e8, respectively.

## Appendix D Disk Angular Momentum

We define the total angular momentum in a Keplerian disk about a protostar with mass  $M_*$  as  $L_{\rm disk}=\int_0^R M(r)V(r)dr$ , where  $V(r)=\sqrt{GM_*/r}$  and  $M(r)=4\pi r^2\rho$ . We assume for simplicity that the gas density  $\rho$  is constant as a function of radius <sup>15</sup>:  $\rho=M_{\rm disk}/4\pi R_{\rm disk}^2$ . Therefore,  $L_{\rm disk}=\int_0^{R_{\rm disk}}G^{0.5}M_*^{0.5}(4\pi\rho)r^{3/2}dr=(2/5)4\pi G^{0.5}M_*^{0.5}\rho R_{\rm disk}^{5/2}=0.4M_{\rm disk}\sqrt{GM_*R_{\rm disk}}$ . If we assume  $R_{\rm disk}=350$  au,  $M_*=20$   $M_\odot$ , and  $M_{\rm disk}=1$   $M_\odot$ , then  $L_{\rm disk}=3\times10^{54}$  g cm<sup>2</sup> s<sup>-1</sup>.

# Appendix E Disks around HMYSOs Known from Previous ALMA Studies

In Table 3, we report the physical properties of known Keplerian disk candidates around HMYSOs observed with ALMA. The list includes seven B-type and seven O-type HMYSOs where Keplerian rotation signatures have been found to date with ALMA observations. Typically, these studies analyze the velocity field of the circumstellar gas as revealed by the line emission of a high-density molecular tracer (e.g., CH<sub>3</sub>CN) and base their claims on two properties: (1) a velocity gradient along the major axis of the source in first-moment maps and (2) a clear

Table 3
Properties of Keplerian Disk Candidates around HMYSOs as Observed with ALMA to Date

Object	Distance (kpc)	Luminosity $(L_{\odot})$	Star Mass $(M_{\odot})$	Disk Mass $(M_{\odot})$	Disk Radius (au)	References
			B-type YSOs			
Orion source I	0.4	$\sim 10^4$	$15\pm2$	< 0.2	75–100	[1, 2]
IRAS 20126+4104	1.6	$\sim 10^4$	12	1.5	860	[3, 4]
IRAS 18162-2048 <sup>a</sup>	1.7	$\sim 10^4$	18	4	300	[5]
G339.88-1.26	2.1	$4 \times 10^{4}$	$11 \pm 5$		430-630	[6]
G35.20-0.74N	2.2	$\sim 10^4$	$18 \pm 3$	3	2500	[7]
G35.03+0.35 A	3.2	$6 \times 10^{3}$	$9 \pm 4$	0.75	2200	[8, 9]
G16.59-0.05	3.6	$3 \times 10^{4}$	$10 \pm 2$	$1.8 \pm 0.3$	500	[10]
			O-type YSOs			
S255IR NIRS3	1.8	$1.6 \times 10^{5b}$	20	0.3	500	[11]
G351.77-0.54	2.2°	$1.7 \times 10^{4}$	14–25 <sup>d</sup>	0.1–0.49 <sup>e</sup>	250–500 <sup>b</sup>	[12]
G17.64+0.16	2.2	$\sim \! 10^{5}$	$45 \pm 10$	< 2.6	120	[13, 14]
IRAS 16547-4247	2.9	$\sim \! 10^{5}$	20	4	870	[15, 16]
G11.92-0.61 MM1	3.4	$\sim 10^{4 \mathrm{f}}$	$34 \pm 5$	2.2-5.8	480	[17]
AFGL 4176	4.2	$\sim \! 10^{5}$	20	2–8	1000	[18, 19]
G023.01-00.41	4.6	$4 \times 10^{4}$	20	1.6	2500	[20]

**Notes.** When mass error bars are not given, the measurements should be taken as loose estimates, e.g., based on consistency checks between a stellar type and the upper-limit luminosity. Radius estimates are wavelength-dependent.

**References.** [1, 2]: Plambeck & Wright (2016), Ginsburg et al. (2018); [3, 4]: Cesaroni et al. (2014), Chen et al. (2016); [5]: Girart et al. (2018); [6]: Zhang et al. (2019); [7]: Sánchez-Monge et al. (2013a); [8, 9]: Beltrán et al. (2014), Beltrán & de Wit (2016); [10]: Moscadelli et al. (2019); [11]: Caratti o Garatti et al. (2017); [12]: Beuther et al. (2017); [13, 14]: Maud et al. (2018, 2019); [15, 16]: Zapata et al. (2019), Tanaka et al. (2020); [17]: Ilee et al. (2018); [18, 19]: Johnston et al. (2015, 2020); [20]: Sanna et al. (2019).

<sup>&</sup>lt;sup>a</sup> Also known as GGD27 MM1, the protostar driving the HH 80/81 jet.

<sup>&</sup>lt;sup>b</sup> Source luminosity increased from  $2.9 \times 10^4$  to  $1.6 \times 10^5$  as a consequence of an accretion burst recorded in 2015 November.

<sup>&</sup>lt;sup>c</sup> The distance to the source is either 1 or 2.2 kpc.

<sup>&</sup>lt;sup>d</sup> Estimated from the source bolometric luminosity through a simulated stellar cluster (Beltrán & de Wit 2016).

<sup>&</sup>lt;sup>e</sup> Depending on the distance to the source assumed.

f The low luminosity in a >30  $M_{\odot}$  YSO could be explained either with the presence of a binary (e.g., two ~15  $M_{\odot}$  YSOs) or with a high accretion rate, which would increase the protostellar radius and decrease its effective temperature (e.g., Hosokawa & Omukai 2009).

<sup>&</sup>lt;sup>15</sup> This is a conservative assumption, since a power law  $\rho \propto r^{-\alpha}$  would give lower L for positive  $\alpha$ , resulting in an even greater flipping (following a substantial dump mass onto the disk) for any realistic disk with  $\alpha = 1$  or 2.

"butterfly" pattern with high-velocity spikes corresponding with the HMYSO position in position—velocity plots.

Table 3 is an update of Table 1 in Rosen et al. (2020). Beltrán (2020) and Johnston et al. (2020) independently reported a slightly different list (13 each) of disk candidates around O-type HMYSOs. Those lists exclude some of the B-type HMYSOs listed in Table 3 but include disk candidates around O-type HMYSOs without Keplerian profile signatures.

## ORCID iDs

```
C. Goddi  https://orcid.org/0000-0002-2542-7743

A. Ginsburg  https://orcid.org/0000-0001-6431-9633

L. T. Maud  https://orcid.org/0000-0002-7675-3565

Q. Zhang  https://orcid.org/0000-0003-2384-6589

Luis A. Zapata  https://orcid.org/0000-0003-2343-7937
```

```
References
Audard, M., Ábrahám, P., Dunham, M. M., et al. 2014, in Protostars and
  Planets VI, ed. H. Beuther et al. (Tuscon, AZ: Univ. Arizona Press), 387
Bally, J., Ginsburg, A., Forbrich, J., & Vargas-González, J. 2020, ApJ, 889, 178
Beltrán, M. 2020, arXiv:2005.06912
Beltrán, M. T., & de Wit, W. J. 2016, A&ARv, 24, 6
Beltrán, M. T., Sánchez-Monge, Á., Cesaroni, R., et al. 2014, A&A, 571, A52
Beuther, H., Walsh, A. J., Johnston, K. G., et al. 2017, A&A, 603, A10
Blandford, R. D., & Payne, D. G. 1982, MNRAS, 199, 883
Boley, P. A., Linz, H., van Boekel, R., et al. 2013, A&A, 558, A24
Bonnell, I. A., & Bate, M. R. 2005, MNRAS, 362, 915
Caratti o Garatti, A., Froebrich, D., Eislöffel, J., Giannini, T., & Nisini, B.
   2008, A&A, 485, 137
Caratti o Garatti, A., Stecklum, B., Garcia Lopez, R., et al. 2017, NatPh,
Cesaroni, R., Sánchez-Monge, Á., Beltrán, M. T., et al. 2017, A&A, 602, A59
Cesaroni, R., Galli, D., Neri, R., & Walmsley, C. M. 2014, A&A, 566, A73
Cesaroni, R., Neri, R., Olmi, L., et al. 2005, A&A, 434, 1039
Chen, H.-R. V., Keto, E., Zhang, Q., et al. 2016, ApJ, 823, 125
Commercon, B., Hennebelle, P., & Henning, T. 2011, ApJL, 742, L9
Cunningham, A. J., Klein, R. I., Krumholz, M. R., & McKee, C. F. 2011, ApJ,
Cunningham, N. J., Moeckel, N., & Bally, J. 2009, ApJ, 692, 943
Frank, A., Ray, T. P., Cabrit, S., et al. 2014, in Protostars and Planets VI, Vol.
   451, ed. H. Beuther et al. (Tuscon, AZ: Univ. Arizona Press)
Frost, A. J., Oudmaijer, R. D., de Wit, W. J., & Lumsden, S. L. 2019, A&A,
   625, A44
Ginsburg, A., Bally, J., Goddi, C., Plambeck, R., & Wright, M. 2018, ApJ,
   860, 119
Ginsburg, A., Glenn, J., Rosolowsky, E., et al. 2013, ApJS, 208, 14
Ginsburg, A., Goddi, C., Kruijssen, J. M. D., et al. 2017, ApJ, 842, 92
Ginsburg, A., Goss, W. M., Goddi, C., et al. 2016, A&A, 595, A27
Girart, J. M., Fernández-López, M., Li, Z. Y., et al. 2018, ApJL, 856, L27
Goddi, C., Ginsburg, A., & Zhang, Q. 2016, A&A, 589, A44
Goddi, C., Greenhill, L. J., Humphreys, E. M. L., Chandler, C. J., &
  Matthews, L. D. 2011a, ApJL, 739, L13
Goddi, C., Henkel, C., Zhang, Q., Zapata, L., & Wilson, T. L. 2015, A&A,
   573, A109
Goddi, C., Humphreys, E. M. L., Greenhill, L. J., Chandler, C. J., &
   Matthews, L. D. 2011b, ApJ, 728, 15
Hartmann, L., & Kenyon, S. J. 1996, ARA&A, 34, 207
Hosokawa, T., Hirano, S., Kuiper, R., et al. 2016, ApJ, 824, 119
Hosokawa, T., & Omukai, K. 2009, ApJ, 691, 823
Hosokawa, T., Yorke, H. W., & Omukai, K. 2010, ApJ, 721, 478
Hull, C. L. H., & Zhang, Q. 2019, FrASS, 6, 3
Hunter, T. R., Brogan, C. L., MacLeod, G., et al. 2017, ApJL, 837, L29
Ilee, J. D., Cyganowski, C. J., Brogan, C. L., et al. 2018, ApJL, 869, L24
Imai, H., Watanabe, T., Omodaka, T., et al. 2002, PASJ, 54, 741
Johnston, K. G., Hoare, M. G., Beuther, H., et al. 2020, A&A, 634, L11
Johnston, K. G., Robitaille, T. P., Beuther, H., et al. 2015, ApJL, 813, L19
Joos, M., Hennebelle, P., Ciardi, A., & Fromang, S. 2013, A&A, 554, A17
Keto, E. 2003, ApJ, 599, 1196
Keto, E., & Wood, K. 2006, ApJ, 637, 850
Klassen, M., Pudritz, R. E., Kuiper, R., Peters, T., & Banerjee, R. 2016, ApJ,
   823, 28
```

```
Koch, P. M., Tang, Y.-W., Ho, P. T. P., et al. 2018, ApJ, 855, 39
Kraus, S., Hofmann, K.-H., Menten, K. M., et al. 2010, Natur, 466, 339
Kraus, S., Kreplin, A., Fukugawa, M., et al. 2017, ApJL, 848, L11
Krumholz, M. R., Klein, R. I., & McKee, C. F. 2007, ApJ, 665, 478
Krumholz, M. R., Klein, R. I., McKee, C. F., Offner, S. S. R., &
   Cunningham, A. J. 2009, Sci, 323, 754
Kuiper, R., Klahr, H., Beuther, H., & Henning, T. 2010, ApJ, 722, 1556
Kuiper, R., Klahr, H., Beuther, H., & Henning, T. 2011, ApJ, 732, 20
Kuiper, R., Turner, N. J., & Yorke, H. W. 2016, ApJ, 832, 40
Leurini, S., Codella, C., López-Sepulcre, A., et al. 2014, A&A, 570, A49
Mangum, J. G., & Shirley, Y. L. 2015, PASP, 127, 266
Marti, J., Rodriguez, L. F., & Reipurth, B. 1995, ApJ, 449, 184
Masson, C. R., & Chernin, L. M. 1993, ApJ, 414, 230
Matsumoto, T., Machida, M. N., & Inutsuka, S.-i. 2017, ApJ, 839, 69
Matthews, L. D., Greenhill, L. J., Goddi, C., et al. 2010, ApJ, 708, 80
Maud, L. T., Cesaroni, R., Kumar, M. S. N., et al. 2018, A&A, 620, A31
Maud, L. T., Cesaroni, R., Kumar, M. S. N., et al. 2019, A&A, 627, L6
Maud, L. T., Tilanus, R. P. J., van Kempen, T. A., et al. 2017, A&A, 605, A121
Meyer, D. M. A., Vorobyov, E. I., Elbakyan, V. G., et al. 2019, MNRAS,
   482, 5459
Meyer, D. M. A., Vorobyov, E. I., Kuiper, R., & Kley, W. 2017, MNRAS,
   464, L90
Moeckel, N., & Goddi, C. 2012, MNRAS, 419, 1390
Moscadelli, L., & Goddi, C. 2014, A&A, 566, A150
Moscadelli, L., Sánchez-Monge, Á., Goddi, C., et al. 2016, A&A, 585, A71
Moscadelli, L., Sanna, A., Cesaroni, R., et al. 2019, A&A, 622, A206
Moscadelli, L., Sanna, A., Goddi, C., et al. 2017, A&A, 600, L8
Myers, A. T., McKee, C. F., Cunningham, A. J., Klein, R. I., &
   Krumholz, M. R. 2013, ApJ, 766, 97
Offner, S. S. R., & Arce, H. G. 2014, ApJ, 784, 61
Pecaut, M. J., & Mamajek, E. E. 2013, ApJS, 208, 9
Pfalzner, S. 2008, A&A, 492, 735
Plambeck, R. L., & Wright, M. C. H. 2016, ApJ, 833, 219
Rivera-Soto, R., Galván-Madrid, R., Ginsburg, A., & Kurtz, S. 2020, ApJ,
Rodríguez, L. F., Dzib, S. A., Zapata, L., et al. 2020, ApJ, 892, 82
Rodríguez, L. F., Porras, A., Claussen, M. J., et al. 2003, ApJL, 586, L137
Rosen, A. L., & Krumholz, M. R. 2020, AJ, 160, 78
Rosen, A. L., Krumholz, M. R., McKee, C. F., & Klein, R. I. 2016, MNRAS,
   463, 2553
Rosen, A. L., Li, P. S., Zhang, Q., & Burkhart, B. 2019, ApJ, 887, 108
Rosen, A. L., Offner, S. S. R., Sadavoy, S. I., et al. 2020, SSRv, 216, 62
Sánchez-Monge, Á., Cesaroni, R., Beltrán, M. T., et al. 2013a, A&A, 552, L10
Sánchez-Monge, Á., López-Sepulcre, A., Cesaroni, R., et al. 2013b, A&A,
  557, A94
Sanchez-Monge, A., Schilke, P., Ginsburg, A., Cesaroni, R., & Schmiedeke, A.
   2018, A&A, 609, A101
Sanna, A., Kölligan, A., Moscadelli, L., et al. 2019, A&A, 623, A77
Sanna, A., Moscadelli, L., Cesaroni, R., et al. 2010, A&A, 517, A71
Sanna, A., Moscadelli, L., Goddi, C., Krishnan, V., & Massi, F. 2018, A&A,
  619, A107
Sato, M., Reid, M. J., Brunthaler, A., & Menten, K. M. 2010, ApJ, 720, 1055
Seifried, D., Banerjee, R., Klessen, R. S., Duffin, D., & Pudritz, R. E. 2011,
         S, 417, 1054
Seifried, D., Banerjee, R., Pudritz, R. E., & Klessen, R. S. 2012, MNRAS,
   423, L40
Seifried, D., Banerjee, R., Pudritz, R. E., & Klessen, R. S. 2013, MNRAS,
   432, 3320
Seifried, D., Banerjee, R., Pudritz, R. E., & Klessen, R. S. 2015, MNRAS,
Shepherd, D. S., Yu, K. C., Bally, J., & Testi, L. 2000, ApJ, 535, 833
Shi, H., Zhao, J.-H., & Han, J. L. 2010b, ApJL, 718, L181
Smith, R. J., Glover, S. C. O., Bonnell, I. A., Clark, P. C., & Klessen, R. S.
            NRAS, 411, 1354
Smith, R. J., Hosokawa, T., Omukai, K., Glover, S. C. O., & Klessen, R. S.
   2012, MNRAS, 424, 457
Tanaka, K. E. I., Tan, J. C., & Zhang, Y. 2016, ApJ, 818, 52
Tanaka, K. E. I., Zhang, Y., Hirota, T., et al. 2020, ApJL, 900, L2
Tobin, J. J., Hartmann, L., Bergin, E., et al. 2012, ApJ, 748, 16
Zapata, L. A., Garay, G., Palau, A., et al. 2019, ApJ, 872, 176
Zapata, L. A., Schmid-Burgk, J., Ho, P. T. P., Rodríguez, L. F., &
   Menten, K. M. 2009, ApJL, 704, L45
Zapata, L. A., Tang, Y.-W., & Leurini, S. 2010, ApJ, 725, 1091
Zhang, Q., Qiu, K., Girart, J. M., et al. 2014, ApJ, 792, 116
Zhang, Y., Tan, J. C., Sakai, N., et al. 2019, ApJ, 873, 73
Zinnecker, H., & Yorke, H. W. 2007, ARA&A, 45, 481
```